Seismic and aseismic fault slip during the initiation phase of the 2017 Mw=6.9 Valparaíso earthquake.

Emmanuel Caballero[1,1,1], Agnes Chounet[2,2,2], Zacharie Duputel[1,1,1], Jorge Jara[3,3,3], Cedric Twardzik[4,4,4], and Romain Jolivet[5,5,5]

[1]Institut de Physique du Globe de Strasbourg, UMR7516, Université de Strasbourg/EOST, CNRS
[2]Institut de Physique du Globe de Strasbourg
[3]Ecole Normale Supérieure de Paris
[4]University of Strasbourg
[5]Ecole Normale Superieure

November 30, 2022

Abstract

Transient deformations associated with foreshocks activity has been observed before large earthquakes, suggesting the occurrence of a detectable pre-seismic slow slip during the initiation phase. In this respect, a critical issue consists in discriminating the relative contributions from seismic and aseismic fault slip during the preparation phase of large earthquakes. We focus on the April-May 2017 Valparaíso earthquake sequence, which involved a Mw=6.9 earthquake preceded by an intense foreshock activity. To assess the relative contribution of seismic and aseismic slip, we compare surface displacements predicted from foreshock source models to the transient motion measured prior to the mainshock. The comparison between observed and predicted displacements shows that only half of the total displacement can be explained by the contribution of foreshocks. This result suggests the presence of aseismic preslip during an initiation phase preceding the mainshock.

Seismic and aseismic fault slip during the initiation phase of the 2017 $M_W = 6.9$ Valparaíso earthquake

Emmanuel Caballero[1], Agnès Chounet[1], Zacharie Duputel[1], Jorge Jara[2], Cedric Twardzik[1], Romain Jolivet[2,3]

[1]Institut de Physique du Globe de Strasbourg, UMR 7516, Université de Strasbourg/EOST, CNRS, Strasbourg, France.
[2]Laboratoire de Géologie, Département de Géosciences, École Normale Supérieure, PSL Université, CNRS UMR 8538, Paris, France
[3]Institut Universitaire de France, 1 rue Descartes, 75005 Paris, France

Key Points:

- The 2017 Valparaíso $M_W = 6.9$ earthquake presents a pre-seismic transient displacement.
- We evaluate the contribution of foreshock-induced displacement to the pre-seismic GPS observations.
- Results suggest that 50±11% of the pre-seismic displacement is caused by aseismic slip.

Corresponding author: Emmanuel Caballero, ecaballeroleyva@unistra.fr

Abstract

Transient deformation associated with foreshocks activity has been observed before large earthquakes, suggesting the occurrence of a detectable pre-seismic slow slip during the initiation phase. A critical issue consists in discriminating the relative contributions from seismic and aseismic fault slip during the preparation phase of large earthquakes. We focus on the April-May 2017 Valparaíso earthquake sequence, which involved a $M_W =$ 6.9 earthquake preceded by intense foreshock activity. To assess the relative contribution of seismic and aseismic slip, we compare surface displacement predicted from foreshocks source models with transient motion measured prior to the mainshock. The comparison between observed and predicted displacements shows that only half of the total displacement can be explained by the contribution of foreshocks. This result suggests the presence of aseismic preslip during an initiation phase preceding the mainshock.

Plain Language Summary

Several studies suggest that some large earthquakes are preceded by aseismic fault slip. Such preslip could explain foreshock activity and transient displacements observed before some large earthquakes. However, a large portion of observed pre-seismic deformations could be associated with the displacement field caused by each individual foreshock earthquakes. This study focuses on the 2017 $M_W = 6.9$ Valparaíso (Chile) earthquake that was preceded by a noticeable GPS displacement and numerous foreshocks. By combining geodetic and seismic observations, our results show that only half of pre-seismic displacement can actually be explained by the contribution of foreshocks. This confirms that the Valparaíso earthquake was preceded by detectable aseismic fault slip accelerating into the main dynamic rupture.

1 Introduction

Experimental and theoretical studies suggest that earthquakes begin with aseismic slow slip accelerating into a dynamic, catastrophic rupture (Das & Scholz, 1981; Kaneko et al., 2016; Latour et al., 2013; Ohnaka, 2000). Laboratory-derived rate-and-state models depict different evolution of preslip within nucleation zones of various sizes (Ampuero & Rubin, 2008; Kaneko & Ampuero, 2011). With technological advances such as high-speed photoelastic techniques, the progressive acceleration from slow stable slip to fast dynamic slip can be accurately monitored in laboratory conditions (e.g., Latour et al., 2013). Despite these advances, the detectability of such nucleation phases on natural faults is still an open question. In addition to the nucleation itself, observations of the precursory phase leading to an earthquake indicate that earthquakes are often preceded by foreshocks that could potentially be triggered by aseismic preslip (Bouchon et al., 2011, 2013; Kato et al., 2012). Nonetheless, the role of foreshocks during this precursory phase remains unclear. At present, two end-member conceptual models compete in explaining the occurrence of foreshocks. In the first model, foreshock stress changes contribute to a slow cascade of random failures, leading eventually to the mainshock (Ellsworth & Bulut, 2018; Helmstetter & Sornette, 2003; Marsan & Enescu, 2012). The second model proposes that foreshocks are triggered by aseismic slip corresponding to the nucleation process of the mainshock (Bouchon et al., 2011; Dodge et al., 1996).

The continued development of geophysical networks in active tectonic regions provides new opportunities to better capture the genesis of earthquakes. Geodetic observations provide strong evidences of pre-seismic transient deformations at various timescales (Ito et al., 2013; Mavrommatis et al., 2014; Ozawa et al., 2012; Socquet et al., 2017; Yokota & Koketsu, 2015). However, the interpretation of such observations is often difficult. This is particularly evident for the 2014 $M_W = 8.4$ Iquique (Chile) earthquake, which was preceded by an active foreshock sequence that started 8 months before the mainshock (Kato & Nakagawa, 2014). This foreshock sequence was accompanied by clear

GPS transient displacements, corresponding at least to some extent to aseismic fault slip preceding the mainshock (S. Ruiz et al., 2014; Socquet et al., 2017). The aseismic behavior of the observed pre-seismic transient is however debated as it might largely correspond to the cumulative co-seismic displacement of the foreshocks and associated afterslip (Bedford et al., 2015; Schurr et al., 2014). A reliable estimate of the relative contribution of seismic and aseismic deformations during nucleation is essential to better capture fault processes at the onset of earthquakes (Herman et al., 2016).

On 24 April 2017, a $M_W = 6.9$ earthquake occurred offshore Valparaíso in the central segment of the Chilean megathrust (33.089°S, 72.116°W, 21:38:28 UTC; Centro Sismólogico National, CSN). This event is relatively moderate given that this region of the Chilean subduction experienced earthquakes of magnitudes $M_W > 8$ (Comte et al., 1986; Dura et al., 2015). This earthquake, however, caught the attention of seismologists because it was preceded by a vigorous foreshock activity in the $\sim$2 days preceding the mainshock. This precursory activity has also been captured by GPS stations indicating a pre-seismic trenchward motion over a similar time-scale (S. Ruiz et al., 2017; J. A. Ruiz et al., 2018). A preliminary analysis of seismological and geodetic observations suggests that 80% of pre-seismic GPS displacement is due to aseismic fault slip preceding the mainshock (S. Ruiz et al., 2017). This first order estimate is obtained by comparing inverted preslip with the seismic moment of foreshocks assuming they are all located on the subduction interface. This assumption is questionable as seismicity catalogs depict a significant dispersion of earthquake locations around the plate interface (S. Ruiz et al., 2017; J. A. Ruiz et al., 2018), most events being located at depths larger than the slab 1.0 model (Hayes et al., 2012). Such dispersion, probably related to depth uncertainty, implies a significant non-random bias in seismic moment for dip-slip earthquakes. For example, if an earthquake at 20 km depth is mislocated at 25 km, the moment is underestimated by nearly 20% using long-period teleseismic records (Tsai et al., 2011). Such mis-estimation of seismic moment may lead to non-negligible errors in the contribution of foreshocks to observed pre-seismic deformations.

The primary goal of this study is to assess the relative contribution of seismic and aseismic slip during the few days preceding the 2017 Valparaíso earthquake. Estimating the seismic contribution to observed geodetic displacement is difficult as we deal with moderate-sized foreshocks ($M_W < 6$) for which a co-seismic offset is not clearly visible on GPS time-series. The seismic contribution to the observed displacement can be estimated by modeling the source of foreshocks from seismic data. However, this process should be done carefully as source models and the corresponding predictions can be affected by significant uncertainties. In this work, we obtain a moment-tensor catalog and predict the corresponding co-seismic offsets at GPS stations accounting for observational and modeling uncertainties. In particular, we account for prediction uncertainties associated with inaccuracies in the Earth model. We find that about half of the observed GPS pre-seismic displacement is aseismic and is caused by preslip in the vicinity of the impending mainshock hypocenter. Such pre-seismic deformation is unlikely to be explained by afterslip induced by preceding foreshocks. This suggests that aseismic preslip played an important role in the 2017 Valparaíso sequence.

2 Pre-seismic Transient Displacements captured by GPS

We process GPS data of 68 stations in South America from several networks (CSN, LIA Montessus de Ballore, Ministerio de Bienes Nacionales, RAMSAC, RBMC-IP, IGS, IGM Bolivia, see supplementary information S1 for references). Processing is done using a differential approach (Herring et al., 2018) including tropospheric delays and horizontal gradients. The results are computed in the ITRF 2014 reference frame (Altamimi et al., 2016) and converted in a fixed South-America frame (Nocquet et al., 2014). We use daily solutions except for the last position before the mainshock, which is obtained from data up to one hour before the event. We remove a trend corresponding to inter-

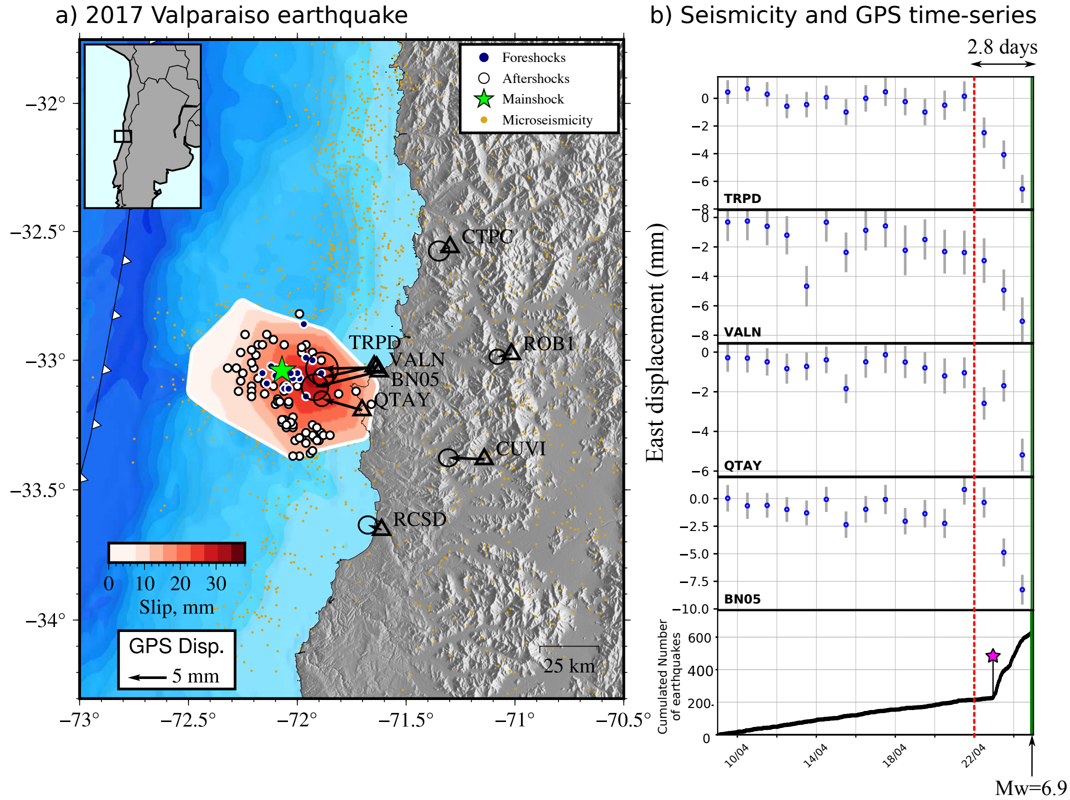

Figure 1. The 2017 Valparaíso earthquake sequence. (a) Earthquake locations including foreshocks (blue circles), mainshock (green star), and aftershocks (white circles). The red colormap indicates the preslip distribution resulting from the inversion of GPS data (see section 5). The black arrows show the cumulative observed GPS surface displacements (up to one hour before the mainshock). Orange dots indicate the seismicity distribution from 2017/01/01 until 2017/10/05 according to the microseismicity catalog obtained by S. Ruiz et al. (2017). (b) GPS Time-series in the vicinity of Valparaíso. The vertical red dashed line indicates approximate onset of the transient displacement visible on the time-series. The cumulative number of earthquakes from S. Ruiz et al. (2017) is shown at the bottom of the figure. The purple star represents the largest $M_W = 6.0$ foreshock.

seismic motion from the time-series by fitting a linear regression in a 4 months time-window before the mainshock. Finally, we subtract the first sample of the time-series (i.e., which we consider as displacement zero) and obtain the corresponding offsets.

Figure 1-b and S3 show the resulting horizontal displacements for stations in the vicinity of the study area. There is a clear westward motion starting about 3 days before the mainshock and reaching $\sim$8 mm close to the coast. Figure 1-b compares GPS time-series with the cumulative number of earthquakes in the micro-seismicity catalog obtained by S. Ruiz et al. (2017). Interestingly, the pre-seismic GPS transient starts before a noticeable increase in seismicity. In Figure 1-b, we can see that the slope of cumulative seismicity rate does not change significantly at the beginning of the transient. The increase in seismicity rate is delayed by about 24 hours and only starts with a $M_W =$ 6.0 foreshock on April 23 (purple star in Figure 1-b). This suggests that aseismic preslip initiated on the fault before the increase in foreshock activity.

3 Centroid Moment Tensor catalog

To constrain the contribution of foreshocks to the observed GPS displacement, we estimate Centroid Moment Tensor (CMT) parameters for moderate to large earthquakes during the Valparaíso earthquake sequence (from 2017/04/05 up to 2017/05/30). We use records from broadband seismic stations located within 12° from the mainshock hypocenter. These stations are mostly included in the C and C1 regional networks maintained by the Centro Sismológico Nacional (CSN) of the Universidad de Chile (Universidad de Chile, 2013). We also use stations operated by GEOSCOPE, and IRIS/USGS network (Institut de Physique du Globe de Paris and Ecole et Observatoire des Sciences de la Terre de Strasbourg (EOST), 1982; Albuquerque Seismological Laboratory (ASL)/USGS, 1993, 1988).

We use a modified version of the W-phase algorithm adapted to regional distances and the magnitude range of the Valparaíso sequence (Kanamori & Rivera, 2008; Zhao et al., 2017). Estimated parameters are the deviatoric moment tensor, the centroid location, the centroid time, and the half-duration of an isosceles triangular moment rate function. The inversion is performed by fitting full waveforms in a 180 s time-window starting at the P-wave. We filter data between 12 s and 100 s using different pass-bands for different magnitude events (see Table S1 in the online supplementary). We compute Green's functions for the source inversion in a 1D layered structure extracted from the 3D Earth model of S. Ruiz et al. (2017) in the area of Valparaíso (Figure S4).

The resulting CMT catalog is shown in Figure 2 and in table S2. Most earthquakes (more than 90% of the total catalog) have thrust mechanisms. Interestingly, foreshocks are mostly concentrated close to the mainshock hypocenter (see Figure 1 and Figure 2-a). On the other hand, aftershocks show a different behavior, surrounding the region where foreshocks have previously occurred.

The cumulative scalar seismic moment released by foreshocks before the mainshock is largely dominated by two events with $M_W \geq 5.5$ (cf., Figure 2-b). These foreshocks of magnitude $M_W = 6.0$ and $M_W = 5.5$ occurred respectively 43 hours and 26 hours before the mainshock. As our CMT catalog only consists of $M_W \geq 3.8$ earthquakes, the contribution of microseismicity is not included in our estimates of cumulative seismic moment before the mainshock. Even though the individual contribution of these small earthquakes to the observed displacement is negligible, their large number may contribute to surface displacement. To assess the contribution of small earthquakes, we consider the frequency-magnitude distribution of our CMT catalog assuming a completeness magnitude of $M_c = 3.9$ (Figure S5). We compare our catalog with previous moment tensor catalogs of the same sequence (S. Ruiz et al., 2017; J. A. Ruiz et al., 2018), which are qualitatively consistent with our estimates (Figure S5). We then compute the Gutenberg-Richter (GR) law using the methodology proposed by Aki (1965) for the whole sequence, and the foreshocks sequence. Even though the GR laws show some discrepancies, they are in good agreement considering the uncertainties on our estimates (Figure S5). The foreshocks GR law is then extrapolated to lower magnitudes, and the cumulative moment of magnitudes below the magnitude of completude is included to correct for the influence of small, hence not detected earthquakes. Our CMT catalog suggests a cumulative moment $M_0 = 1.474 \times 10^{18}$ N·m. The cumulative seismic moment of foreshocks with magnitudes below completeness is $M_0 = 4.966 \times 10^{15}$ N·m (i.e., $M_w = 4.4$). The contribution of microearthquakes is therefore negligible compared to seismic events.

To evaluate the contribution of foreshocks to observed surface displacements, we calculate synthetic static displacements using our CMT catalog and the same 1D velocity model employed to obtain our CMT solutions. Synthetics are computed using the CSI package (http://www.geologie.ens.fr/ jolivet/csi) incorporating the approach of Zhu and Rivera (2002) to compute static displacement in a layered model. Results on Figure S6 indicate that the largest foreshock ($M_W = 6.0$) largely dominates the co-seismic

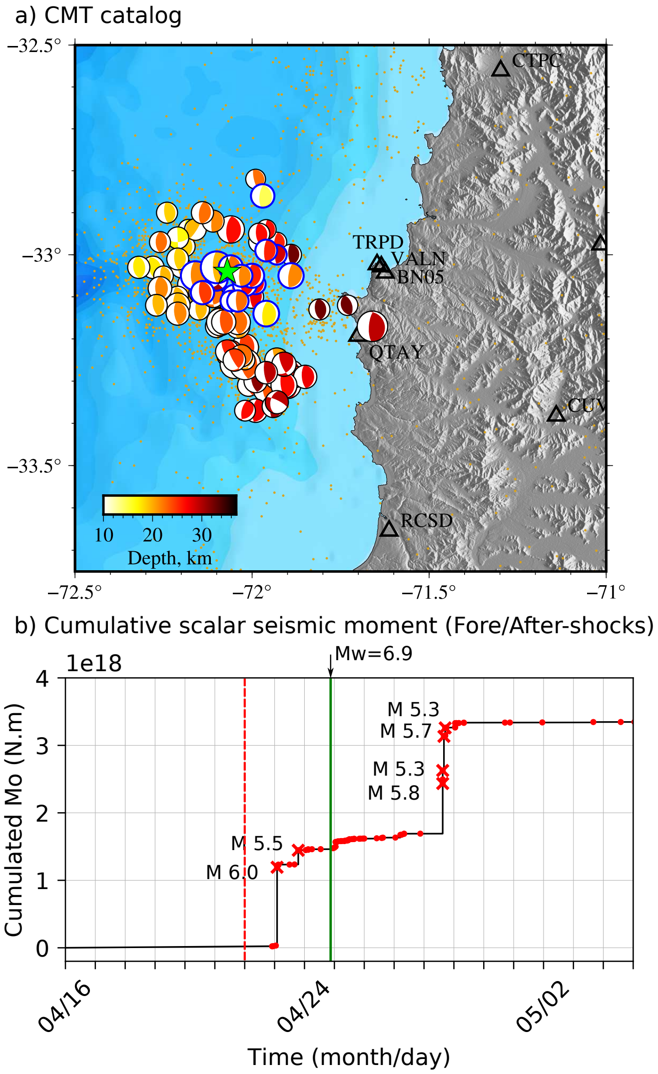

Figure 2. CMT solutions of the 2017 Valparaíso earthquake sequence and cumulative moment (a) CMT solutions of the 2017 Valparaíso earthquake sequence. Focal mechanisms are contoured in blue and black for foreshocks and aftershocks respectively. The size of beach balls scales with the moment magnitude. Color of the compressive quadrants represents the event depth. (b) Cumulative scalar seismic moment of the 2017 Valparaíso sequence. The mainshock scalar moment is not included in this figure. The red dashed line outlines the approximate onset of transient displacements visible on GPS time-series. The green line indicates the origin time.

contribution to the observed GPS transient while $M_W < 6.0$ events in our catalog generate relatively small surface displacement. Assuming that microearthquakes are located in the vicinity of $M_W \geq 3.8$ foreshocks, they should also have a negligible contribution to the observed surface displacement (given their small cumulative scalar moment). As the $M_W = 6.0$ foreshock plays a important role in the sequence, we assess uncertainties associated with the corresponding CMT parameters.

4 Uncertainty on predicted co-seismic displacements

Synthetic co-seismic surface displacements are sensitive to uncertain earthquake source parameters. For large magnitude foreshocks, uncertainties on centroid location and moment tensor affect our estimates of the co-seismic contribution to the transient displacement observed before the mainshock. Source parameters uncertainties can either result from observational errors, or from errors in the forward model (prediction/theoretical errors). For example, there might be innacuracies in the velocity model, which is known to induce non-negligible errors in CMT solutions (Duputel et al., 2012, 2014; Morales-Yañez et al., 2020). The point source assumption is another source of uncertainty in the forward model. As for the observations, temporally and spatially variable noise level at seismic stations is a major source of uncertainty.

In order to assess uncertainties associated with the CMT solution of the largest $M_W = 6.0$ foreshock, we perform a new CMT inversion within a Bayesian framework, following Duputel et al. (2012, 2014). Each source of uncertainty considered here is integrated in the problem as a covariance matrix. The covariance matrix C_d, associated with observational errors, is derived after a first CMT inversion. From this inversion, an average correlation function is derived from residuals between synthetic and observed waveforms at each station. This allows us to estimate the correlation between neighbor data samples, and include it into C_d. The standard deviation for each channel is fixed to 4 times the corresponding average absolute residuals. This empirical procedure provides a conservative estimate of observational uncertainty associated with each waveform.

Forward modeling uncertainties are represented by the matrix C_p, which assesses the influence of inaccuracies in the Earth model. We use the same velocity model as in section 3 assuming log-normal uncertainties on elastic parameters as shown in Figure S4. Uncertainty in each layer is estimated by assessing the spatial variability of the 3D Earth model of S. Ruiz et al. (2017) in the epicentral region and by comparison with other regional models (e.g., J. A. Ruiz et al., 2018). To evaluate the corresponding variability in the predictions, we employ the first-order perturbation approach described in Duputel et al. (2014), assuming that prediction error is linearly related with uncertainty on the elastic parameters. A test is described in supplementary information S2 and Figures S7-S8 to assess the validity of this approach.

The posterior ensemble of plausible source locations and moment tensors is appraised using a strategy similar to Sambridge (1999). At a fixed point-source location in time and space, the posterior distribution of moment tensor parameters is Gaussian and can be written as (Tarantola et al., 1982):

$$p(\mathbf{m}|\mathbf{d}_{obs}, \mathbf{x}) = N(\widetilde{\mathbf{m}}, \widetilde{\mathbf{C}}_m) \tag{1}$$

where $\mathbf{m}$ are the moment tensor parameters, $\mathbf{d}_{obs}$ is the data vector containing the concatenated observed waveforms and $\mathbf{x}$ is the point source location. The right-hand member of this equation is a Gaussian distribution of mean $\widetilde{\mathbf{m}}$ and covariance $\widetilde{\mathbf{C}}_m$. The posterior mean $\widetilde{\mathbf{m}}$ is the maximum *a posteriori* moment tensor given by:

$$\widetilde{\mathbf{m}} = \left(\mathbf{G}^t \mathbf{C}_\chi^{-1} \mathbf{G}\right)^{-1} \mathbf{G}^t \mathbf{C}_\chi^{-1} \mathbf{d}_{obs}, \tag{2}$$

where $\mathbf{G}$ is the Green's function matrix while $\mathbf{C}_\chi = \mathbf{C}_d + \mathbf{C}_p$ is the covariance matrix reflecting observational ($\mathbf{C}_d$) and prediction uncertainties ($\mathbf{C}_p$). The posterior covariance matrix is given by:

$$\widetilde{\mathbf{C}}_m = \left(\mathbf{G}^t \mathbf{C}_\chi^{-1} \mathbf{G}\right)^{-1} \tag{3}$$

To get the joint posterior distribution on moment tensor $\mathbf{m}$ and source location $\mathbf{x}$, we first calculate $\widetilde{\mathbf{m}}$ and $\widetilde{\mathbf{C}}_m$ on a 3D grid of possible point-source locations around the hypocenter. Starting from the initial location $\mathbf{x}_c$ determined in section 3 (corresponding a moment tensor $\mathbf{m}_c$), we then employ an hybrid metropolis algorithm by repeating the following iterations until a sufficiently large number of model samples is generated:

1. Randomly generate a candidate point-source location $\mathbf{x}^* = \mathbf{x}_c + \delta\mathbf{x}$ where $\delta\mathbf{x}$ is a small perturbation randomly generated from a Gaussian distribution with a standard deviation of 0.1° in latitude/longitude and σ=0.1 km in depth.
2. Extract $\widetilde{\mathbf{m}}$ and $\widetilde{\mathbf{C}}_m$ from the grid point closest to $\mathbf{x}^*$ and generate a random model $\mathbf{m}^*$ from $p(\mathbf{m}|\mathbf{d}_{obs}, \mathbf{x}^*)$ in eq. (1).
3. Accept or reject $\mathbf{m}^*$ and $\mathbf{x}^*$ using a standard Metropolis approach:
   - Draw a random number $\alpha \sim U(0, 1)$
   - Accept $\mathbf{m}^*$ and $\mathbf{x}^*$ if $\alpha < \min\left(1, \frac{p(\mathbf{m}|\mathbf{d}_{obs},\mathbf{x}^*)}{p(\mathbf{m}_c|\mathbf{d}_{obs},\mathbf{x}_c)}\right)$.
   - Otherwise duplicate $\mathbf{m}_c$ and $\mathbf{x}_c$

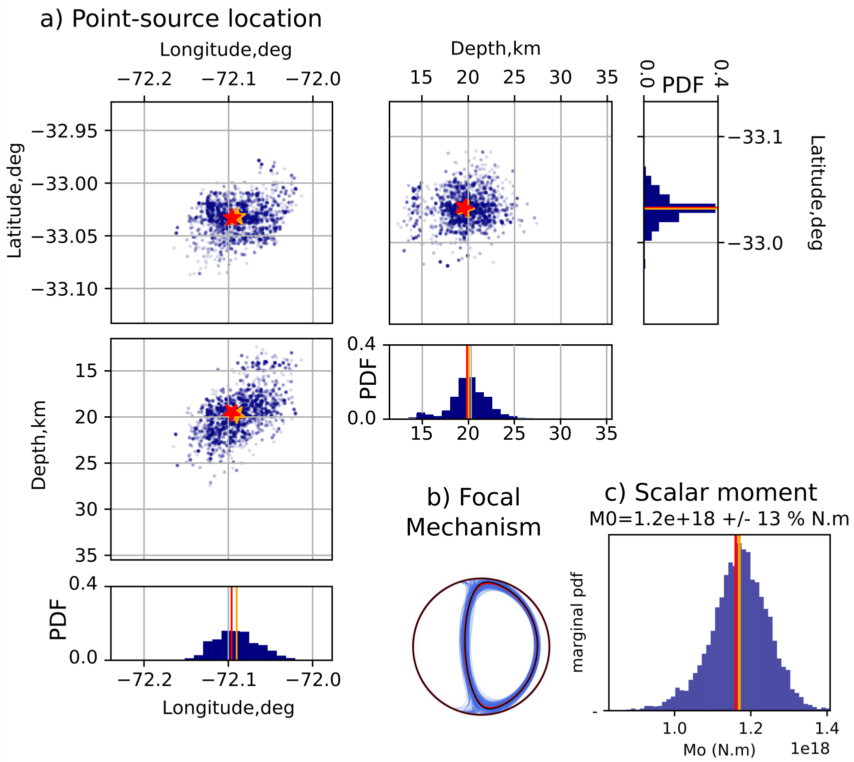

Figure 3. Bayesian point-source model for the M_W=6.0 foreshock on 2017-04-23. Blue circles and lines in the figure represent model samples randomly drawn from the posterior distribution. a) Samples from the posterior PDF depecting uncertainties in the point source location. The red and orange stars are the initial solution (i.e. starting model) and the posterior mean model respectively. b) Focal mechanism uncertainty. c) Marginal posterior PDF of the scalar seismic moment. The red and orange lines are the initial and the posterior mean model.

Figure 3 shows 4500 model samples generated using the approach described above. The posterior distribution shows a location uncertainty of about 10 km. We observe a good fit between observed and synthetic seismograms (Figure S9). However, we also notice a trade-off between longitude and depth, which probably results from the distribution of stations used for inversion (Figure S10). To evaluate the uncertainty on the predicted co-seismic displacement, we simulate static displacement for each model samples shown in Figure 3. The resulting stochastic co-seismic displacements are shown in Gray in Figure 4a for GPS stations that are closest to the mainshock epicenter. This shows prediction uncertainties ranging from 0.25 to 0.4 mm on the east component of displacement. Despite these uncertainties, the predicted cumulative co-seismic offsets are still significantly smaller than the observed pre-seismic displacements ($\sim$ 6 to 8 mm of the east component for the closest stations).

5 Partitioning between seismic and aseismic fault slip

In Figure 4, we compare the total cumulative foreshock co-seismic offset with the observed pre-seismic GPS displacement. Predicted co-seismic displacements include the contribution of microearthquakes below the magnitude of completeness, assuming a total scalar moment derived from our GR analysis with a location and mechanism similar to the $M_W = 6.0$ foreshock. As discussed earlier, only the largest foreshock $M_W = 6.0$ is significantly contributing to co-seismic displacements (see Figure 4a and S6). The contribution of earthquakes smaller than $M_W = 6.0$ has a minimal impact on the final result.

To get a total budget of seismic and aseismic displacement before the mainshock, Figure 4b compares GPS data 1 hour before the mainshock with the corresponding cumulative foreshock displacement. Observed displacement are on average between 4 and 6 mm larger than co-seismic offsets. Such differences cannot be explained by uncertainties on the observations and the predictions. These results clearly suggest that a significant portion of the observed pre-seismic deformation is actually aseismic and cannot be caused by foreshocks. We estimate that about 51$\pm$11% of the displacement measured at the GPS stations originates from aseismic slip on the megathrust. As shown in Figure,4c, the portion of aseismic deformation is quite consistent between stations suggesting that a common source located in the vicinity of the foreshocks could explain those results.

To further explore this hypothesis, we then conduct two inversions: a first slip inversion of the total GPS pre-seismic displacement and another inversion after removing the contribution of foreshocks (i.e., aseismic displacement only). To build a fault geometry, we use the CSI package to mesh the *Slab 2.0* model with triangles of variable sizes as shown in Figure 4e-f. We invert for slip values at the triangular nodes using AlTar, a Markov chain Monte Carlo sampler based on the algorithm described by Minson et al. (2013). Continuous fault slip distribution is represented as a linear interpolation of the slip values at the triangular nodes. Green's functions are computed in the same stratified elastic model used for our CMT catalog (Figure S4). Given the limited amount of available observations, we enforce a positive Laplacian prior distribution with a scale parameter of 1 m. Such sparsity-inducing prior will favor "simple" models with slip only where it is requested by the data. Results in Figure 4e-f shows that GPS observations can be explained by slip in the vicinity of the mainshock hypocenter. Aseismic slip distribution appears to be somewhat more spread out, which may be an effect of the larger uncertainty associated with GPS data after removing the contribution of foreshocks (as the co-seismic prediction uncertainty propagates in the corrected GPS data).

6 Discussion and conclusion

We investigate the seismic and aseismic motions during the preparation phase of the 2017 $M_w = 6.9$ Valparaíso earthquake. We first evaluate the contribution of foreshock-induced displacement to pre-seismic GPS observations. Co-seismic offsets are largely dominated by a $M_W = 6.0$ foreshock that occurred $\sim$43 hours before the mainshock. As pointed out in section 2, the transient GPS signal starts before the increase in seismicity rate. More specifically, we can see in Figure 4a that the observed displacement on April 22 mainly corresponds to aseismic slip as no significant foreshock occurs on that day. On the other hand, the position on April 23 results from a combination of seismic and aseismic fault slip. The detailed evolution of the partitioning between seismic and aseismic slip is difficult to interpret using daily GPS time-series in which each position corresponds to an average over 24 hours. This analysis is also subject to large observational and pre-

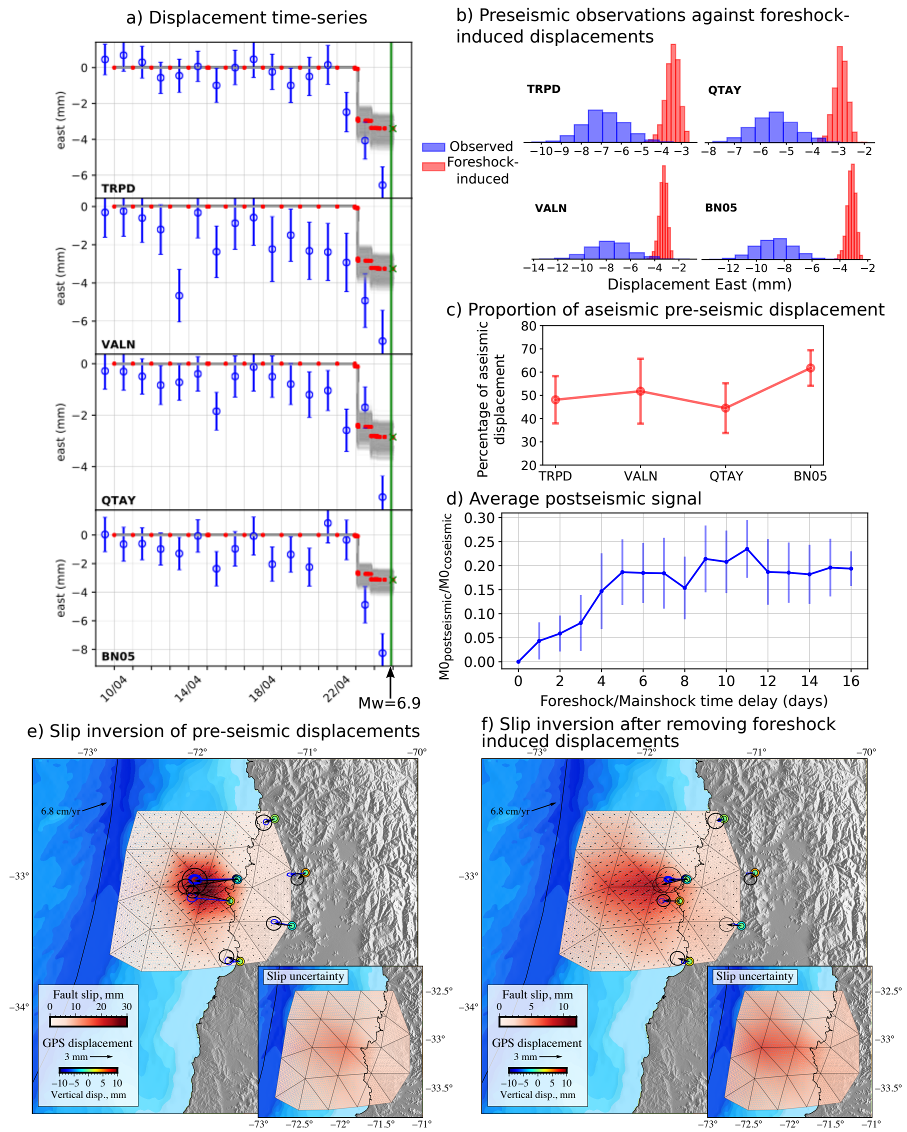

Figure 4. Slip during the Valparaíso foreshock sequence. a) Time series of GNSS data (blue) and stochastic foreshock-induced co-seismic displacement (gray). Red dots represent the average of stochastic co-seismic offsets. Green cross corresponds to the total foreshock displacement, including the contribution of earthquakes below the magnitude of completeness. b) Distributions of observed pre-seismic displacement and predicted cumulative co-seismic offsets caused by foreshocks. Blue histograms represent observations assuming Gaussian uncertainties from standard errors estimated at each station. Red histograms correspond to the posterior distribution of cumulative foreshock-induced co-seismic displacement. c) Percentage of aseismic displacement for each station. d) Average postseismic signal measured on stations TRPD, VALN, BN05 and QTAY (see Figure S11). e) Slip inversion of pre-seismic GPS data. f) Slip inversion of GPS data after removing foreshock-induced displacement. Black and blue arrows are observed and predicted horizontal GPS displacements along with their 1-σ ellipses (representing observational and prediction uncertainties, respectively). Colored circles are observed (outer circles) and predicted (inner circles) vertical displacements from GPS and tide gauges, respectively.

diction uncertainties. For these reasons, we focus on the overall partitioning between seismic and aseismic slip during the preparation phase of the Valparaíso earthquake.

Our analysis shows that a significant part of pre-seismic GPS observations are not explained by foreshock-induced displacement even when accounting for prediction and observation uncertainties. We estimate that $\sim 50 \pm 11\%$ of GPS displacements is likely caused by aseismic slip, a ratio that is fairly consistent for different stations in the vicinity of the Valparaíso sequence (Figure 4c). To check weather such pre-seismic motion could be explained by slip on the plate interface, we conduct a slip inversion after correcting GPS data from foreshock-induced displacement (cf., Figure 4f). The distribution of aseismic preslip spreads toward the west of Valparaíso city with an extension of about 50×90 km and a scalar moment of $M_0 = 3.08 \times 10^{18}$ N.m (i.e., $M_w = 6.26$). This aseismic motion represents about 50% of the moment calculated for the slip model derived from uncorrected GPS data ($M_0 = 5.67 \times 10^{18}$ N.m, Figure 4e). Given the cumulative moment of foreshocks ($M_0 = 1.48 \times 10^{18}$ N.m), we estimate that nearly 70% of the scalar moment released during the preparation phase of the Valparaíso mainshock is aseismic, which is roughly in agreement with estimates from S. Ruiz et al. (2017). The smaller portion of aseismic moment derived from the comparison of slip models in Figure 4e-f likely results from the simplistic assumption in Figure 4e that all foreshocks are located on the plate interface.

Even if our analysis demonstrates the existence of aseismic slip prior to the Valparaíso mainshock, such aseismic motion may include afterslip from preceding bursts of seismicity. This has been suggested for pre-seismic displacement observed before the 2014 $M_W = 8.1$ Iquique earthquake, which could potentially be explained by afterslip induced by foreshock seismicity (Bedford et al., 2015). Testing such possibility for the 2017 Valparaíso sequence is difficult as we cannot easily isolate the afterslip signal from GPS time-series, which likely incorporate other contributions including preslip of the impeding mainshock. To assess the contribution of afterslip, we employ two approaches. In a first approach, we use the mainshock post-seismic GPS signals as a proxy for the afterslip induced by foreshocks. The mainshock post-seismic time-series are normalized by the co-seismic offset of each station to evaluate the relative proportion of post-seismic displacement as a function of time. This suggests that about 10% of the co-seismic moment after 43 hours corresponds to post-seismic deformations (see Figure 4d and Figure S11). This result is consistent with values reported for earthquakes with similar or larger magnitudes (Chlieh et al., 2007; D'agostino et al., 2012; Lin et al., 2013). If we assume a similar behavior for the foreshocks, the post-seismic signal caused by foreshocks is below measurement uncertainties (approximately 0.7 mm for an uncertainty of 1.1 mm in GPS signals) and can therefore be neglected. In a second approach, we make the more conservative assumption that afterslip caused by foreshocks is totally released before the mainshock. Following the empirical scaling relationship $M_{0(postseismic)}/M_{0(coseismic)} = 0.36 + / - 0.2$ proposed by Alwahedi and Hawthorne (2019), the aseismic displacement not related to foreshocks is reduced to about $37\% + / - 13\%$ of the total pre-seismic GPS observations (Figure S12). The total observed displacement is therefore unlikely to be explained by the contribution of foreshocks even when adding the associated afterslip. Such evaluation should be taken with caution due to the non-linear nature of the relationship between slip rate and co-seismic stress change for afterslip (e.g., Perfettini & Avouac, 2004; Perfettini et al., 2010).

Diverse numerical and experimental studies bring up the potential importance of aseismic preslip in the triggering of foreshocks (e.g., Kaneko et al., 2016; McLaskey & Kilgore, 2013). If such observations apply on natural faults, foreshock locations could potentially inform us about the overall spatial extent of the nucleation zone prior to an earthquake. This idea is in fairly good agreement with our results suggesting a first-order correlation between preslip distribution and the location of foreshocks (Figure 1 and Figure 4). Even if preslip appears to be an important mechanism in the triggering of foreshocks, part of the foreshock activity likely results from cascading phenomena due to stress changes of neighboring events. In addition, we still need to understand why most earthquakes are not preceded by foreshock activity and even less with observable pre-seismic motion. This lack of systematic precursory activity might partly be due to an observational gap due to the incompleteness of current seismicity catalog (as suggested by Mignan, 2014) or the lack of near fault geodetic observations prior to large earthquakes. The analysis of an highly complete earthquake catalog in Southern California showed that 72% of $M_W \geq 4$ earthquakes in the region are preceded by an elevated seismic activity compared with the background seismicity rate (Trugman & Ross, 2019), suggesting that foreshock activity is more ubiquitous than previously thought. However, a recent reanalysis of the same catalog suggested that a much smaller portion of these foreshock sequences were really anomalous and could not be attributed to temporal fluctuations in background seismicity rate (van den Ende & Ampuero, 2020). Although anomalous foreshock sequences currently appears to be the exceptional, the improvement of near-fault geodetic and seismological observational capabilities are essential to bridge the gap between natural fault observations and laboratory experiments, where foreshocks are commonly observed.

Acknowledgments

We thank J. Ruiz, S. Ruiz, L. Rivera and J. C. Baez for helpful discussion. This project has received funding from the European Research Council (ERC, under the European Union's Horizon 2020 research and innovation programme under grant agreement No. 805256 and grant agreement No 758210) and from Agence Nationale de la Recherche (project ANR-17-ERC3-0010). This research was also supported by the Mexican National Council for Science and Technology (CONACYT), scholarship 2018-000003-01EXTF-00012. RJ acknowledges funding from the Institut Universitaire de France. The seismological data used in this study were acquired by CSN, GEOSCOPE and IRIS/USGS are freely accessible through the IRIS DMC (https://service.iris.edu/). The authors thank to Instituto Geográfico Militar of Bolivia (http://www.igmbolivia.gob.bo), The International GNSS (http://www.igs.org), Instituto Brasileiro de Geografia e Estatistica (http://www.ibge.gov.br), Instituto Geográfico Nacional de Argentina (http://www.ign.gob.ar), Laboratoire International Associé "Montessus de Ballore" (http://www.lia-mb.net), Ministerio de Bienes Nacionales de Chile (www.bienesnacionales.cl) and the Centro Sismológico Nacional de Chile (http://www.csn.uchile.cl) for making the raw GNSS data available. GNSS data are available via the URLs listed above. We thank an anonymous reviewer, Piero Poli, and Editor Germán Prieto for their valuable comments which improved this manuscript.

References

Aki, K. (1965). Maximum likelihood estimate of b in the formula log n= a-bm and its confidence limits. *Bull. Earthq. Res. Inst., Tokyo Univ.*, *43*, 237–239.

Albuquerque Seismological Laboratory (ASL)/USGS. (1988). *Global seismograph network - iris/usgs (gsn). international federation of digital seismograph networks.* doi: https://doi.org/10.7914/SN/IU

Albuquerque Seismological Laboratory (ASL)/USGS. (1993). *Global telemetered seismograph network (usaf/usgs). international federation of digital seismograph networks.* doi: https://doi.org/10.7914/SN/GT

Altamimi, Z., Rebischung, P., Métivier, L., & Collilieux, X. (2016). ITRF2014: A new release of the International Terrestrial Reference Frame modeling nonlinear station motions. *Journal of Geophysical Research: Solid Earth*, *121*(8), 6109–6131. doi: 10.1002/2016JB013098

Alwahedi, M. A., & Hawthorne, J. C. (2019). Intermediate-magnitude postseismic slip follows intermediate-magnitude (m 4 to 5) earthquakes in california. *Geophysical Research Letters*, *46*(7), 3676–3687.

Ampuero, J.-P., & Rubin, A. M. (2008). Earthquake nucleation on rate and state faults–aging and slip laws. *Journal of Geophysical Research: Solid Earth*, *113*(B1).

Bedford, J., Moreno, M., Schurr, B., Bartsch, M., & Oncken, O. (2015). Investigating the final seismic swarm before the iquique-pisagua 2014 mw 8.1 by comparison of continuous gps and seismic foreshock data. *Geophysical Research Letters*, *42*(10), 3820–3828.

Bouchon, M., Durand, V., Marsan, D., Karabulut, H., & Schmittbuhl, J. (2013). The long precursory phase of most large interplate earthquakes. *Nature geoscience*, *6*(4), 299–302.

Bouchon, M., Karabulut, H., Aktar, M., Özalaybey, S., Schmittbuhl, J., & Bouin, M.-P. (2011). Extended nucleation of the 1999 mw 7.6 izmit earthquake. *science*, *331*(6019), 877–880.

Chlieh, M., Avouac, J.-P., Hjorleifsdottir, V., Song, T.-R. A., Ji, C., Sieh, K., ... others (2007). Coseismic slip and afterslip of the great mw 9.15 sumatra–andaman earthquake of 2004. *Bulletin of the Seismological Society of America*, *97*(1A), S152–S173.

Comte, D., Eisenberg, A., Lorca, E., Pardo, M., Ponce, L., Saragoni, R., ... Suárez, G. (1986). The 1985 central chile earthquake: A repeat of previous great earthquakes in the region? *Science*, *233*(4762), 449–453.

D'agostino, N., Cheloni, D., Fornaro, G., Giuliani, R., & Reale, D. (2012). Space-time distribution of afterslip following the 2009 l'aquila earthquake. *Journal of Geophysical Research: Solid Earth*, *117*(B2).

Das, S., & Scholz, C. (1981). Theory of time-dependent rupture in the earth. *Journal of Geophysical Research: Solid Earth*, *86*(B7), 6039–6051.

Dodge, D. A., Beroza, G. C., & Ellsworth, W. (1996). Detailed observations of california foreshock sequences: Implications for the earthquake initiation process. *Journal of Geophysical Research: Solid Earth*, *101*(B10), 22371–22392.

Duputel, Z., Agram, P. S., Simons, M., Minson, S. E., & Beck, J. L. (2014). Accounting for prediction uncertainty when inferring subsurface fault slip. *Geophysical Journal International*, *197*(1), 464–482.

Duputel, Z., Rivera, L., Fukahata, Y., & Kanamori, H. (2012). Uncertainty estimations for seismic source inversions. *Geophysical Journal International*, *190*(2), 1243–1256.

Dura, T., Cisternas, M., Horton, B. P., Ely, L. L., Nelson, A. R., Wesson, R. L., & Pilarczyk, J. E. (2015). Coastal evidence for holocene subduction-zone earthquakes and tsunamis in central chile. *Quaternary Science Reviews*, *113*, 93–111.

Ellsworth, W. L., & Bulut, F. (2018). Nucleation of the 1999 izmit earthquake by a triggered cascade of foreshocks. *Nature Geoscience*, *11*(7), 531–535.

Hayes, G. P., Wald, D. J., & Johnson, R. L. (2012). Slab1.0: A three-dimensional model of global subduction zone geometries. *Journal of Geophysical Research: Solid Earth*, *117*(B1). Retrieved from https://agupubs.onlinelibrary.wiley.com/doi/abs/10.1029/2011JB008524 doi: 10.1029/2011JB008524

Helmstetter, A., & Sornette, D. (2003). Foreshocks explained by cascades of triggered seismicity. *Journal of Geophysical Research: Solid Earth*, *108*(B10).

Herman, M. W., Furlong, K. P., Hayes, G. P., & Benz, H. M. (2016). Foreshock triggering of the 1 april 2014 mw 8.2 iquique, chile, earthquake. *Earth and Planetary Science Letters*, *447*, 119–129.

Herring, T. A., King, R., Floyd, M., & McClusky, S. C. (2018). GAMIT Reference Manual. GPS Analysis at MIT GLOBK, Release 10.7. (June), 168.

Institut de Physique du Globe de Paris and Ecole et Observatoire des Sciences de la Terre de Strasbourg (EOST). (1982). *Geoscope - french global network of broadband seismic stations.* doi: https://doi.org/10.18715/GEOSCOPE.G

Ito, Y., Hino, R., Kido, M., Fujimoto, H., Osada, Y., Inazu, D., ... others (2013). Episodic slow slip events in the japan subduction zone before the 2011 tohoku-oki earthquake. *Tectonophysics*, *600*, 14–26.

Kanamori, H., & Rivera, L. (2008). Source inversion ofwphase: speeding up seismic tsunami warning. *Geophysical Journal International*, *175*(1), 222–238.

Kaneko, Y., & Ampuero. (2011, November). A mechanism for preseismic steady rupture fronts observed in laboratory experiments. *Geophys. Res. Lett.*, *38*(21), n/a–n/a.

Kaneko, Y., Nielsen, S. B., & Carpenter, B. M. (2016). The onset of laboratory earthquakes explained by nucleating rupture on a rate-and-state fault. *Journal of Geophysical Research: Solid Earth*, *121*(8), 6071–6091.

Kato, A., & Nakagawa, S. (2014). Multiple slow-slip events during a foreshock sequence of the 2014 iquique, chile mw 8.1 earthquake. *Geophysical Research Letters*, *41*(15), 5420–5427.

Kato, A., Obara, K., Igarashi, T., Tsuruoka, H., Nakagawa, S., & Hirata, N. (2012). Propagation of slow slip leading up to the 2011 mw 9.0 tohoku-oki earthquake. *Science*, *335*(6069), 705–708.

Latour, S., Schubnel, A., Nielsen, S., Madariaga, R., & Vinciguerra, S. (2013). Characterization of nucleation during laboratory earthquakes. *Geophysical Research Letters*, *40*(19), 5064–5069.

Lin, Y.-n. N., Sladen, A., Ortega-Culaciati, F., Simons, M., Avouac, J.-P., Fielding, E. J., ... others (2013). Coseismic and postseismic slip associated with the 2010 maule earthquake, chile: Characterizing the arauco peninsula barrier effect. *Journal of Geophysical Research: Solid Earth*, *118*(6), 3142–3159.

Marsan, D., & Enescu, B. (2012). Modeling the foreshock sequence prior to the 2011, mw9.0 tohoku, japan, earthquake. *Journal of Geophysical Research: Solid Earth*, *117*(B6).

Mavrommatis, A. P., Segall, P., & Johnson, K. M. (2014). A decadal-scale deformation transient prior to the 2011 mw 9.0 tohoku-oki earthquake. *Geophysical Research Letters*, *41*(13), 4486–4494.

McLaskey, G. C., & Kilgore, B. D. (2013). Foreshocks during the nucleation of stick-slip instability. *Journal of Geophysical Research: Solid Earth*, *118*(6), 2982–2997.

Mignan, A. (2014). The debate on the prognostic value of earthquake foreshocks: A meta-analysis. *Scientific Reports*, *4*(1), 4099–5.

Minson, S., Simons, M., & Beck, J. (2013). Bayesian inversion for finite fault earthquake source models i—theory and algorithm. *Geophysical Journal International*, *194*(3), 1701–1726.

Morales-Yañez, C., Duputel, Z., & Rivera, L. (2020). Impact of 3d earth structure on w-phase cmt parameters. *Geophysical Journal International*.

Nocquet, J. M., Villegas-Lanza, J. C., Chlieh, M., Mothes, P. A., Rolandone, F., Jarrin, P., ... Yepes, H. (2014). Motion of continental slivers and creeping subduction in the northern Andes. *Nature Geoscience*, *7*(4), 287–291. doi: 10.1038/ngeo2099

Ohnaka, M. (2000). A physical scaling relation between the size of an earthquake and its nucleation zone size. *pure and applied geophysics*, *157*(11-12), 2259–2282.

Ozawa, S., Nishimura, T., Munekane, H., Suito, H., Kobayashi, T., Tobita, M., & Imakiire, T. (2012). Preceding, coseismic, and postseismic slips of the 2011 tohoku earthquake, japan. *Journal of Geophysical Research: Solid Earth*, *117*(B7).

Perfettini, H., & Avouac, J.-P. (2004). Postseismic relaxation driven by brittle creep: A possible mechanism to reconcile geodetic measurements and the decay rate of aftershocks, application to the chi-chi earthquake, taiwan. *Journal of Geophysical Research: Solid Earth*, *109*(B2).

Perfettini, H., Avouac, J.-P., Tavera, H., Kositsky, A., Nocquet, J.-M., Bondoux, F., ... others (2010). Seismic and aseismic slip on the central peru megathrust.

Nature, *465*(7294), 78–81.

Ruiz, J. A., Contreras-Reyes, E., Ortega-Culaciati, F., & Manríquez, P. (2018). Rupture process of the april 24, 2017, mw 6.9 valparaíso earthquake from the joint inversion of teleseismic body waves and near-field data. *Physics of the Earth and Planetary Interiors*, *279*, 1–14.

Ruiz, S., Aden-Antoniow, F., Baez, J., Otarola, C., Potin, B., del Campo, F., … others (2017). Nucleation phase and dynamic inversion of the mw 6.9 valparaíso 2017 earthquake in central chile. *Geophysical Research Letters*, *44*(20), 10–290.

Ruiz, S., Metois, M., Fuenzalida, A., Ruiz, J., Leyton, F., Grandin, R., … Campos, J. (2014). Intense foreshocks and a slow slip event preceded the 2014 iquique mw 8.1 earthquake. *Science*, *345*(6201), 1165–1169.

Sambridge, M. (1999). Geophysical inversion with a neighbourhood algorithm—ii. appraising the ensemble. *Geophysical Journal International*, *138*(3), 727–746.

Schurr, B., Asch, G., Hainzl, S., Bedford, J., Hoechner, A., Palo, M., … others (2014). Gradual unlocking of plate boundary controlled initiation of the 2014 iquique earthquake. *Nature*, *512*(7514), 299–302.

Socquet, A., Valdes, J. P., Jara, J., Cotton, F., Walpersdorf, A., Cotte, N., … Norabuena, E. (2017). An 8 month slow slip event triggers progressive nucleation of the 2014 chile megathrust. *Geophysical Research Letters*, *44*(9), 4046–4053.

Tarantola, A., Valette, B., et al. (1982). Inverse problems= quest for information. *Journal of geophysics*, *50*(1), 159–170.

Trugman, D. T., & Ross, Z. E. (2019, August). Pervasive Foreshock Activity Across Southern California. *Geophys. Res. Lett.*, *46*(15), 8772–8781. Retrieved 2019-12-23, from `https://onlinelibrary.wiley.com/doi/abs/10.1029/2019GL083725` doi: 10.1029/2019GL083725

Tsai, V. C., Hayes, G. P., & Duputel, Z. (2011, April). Constraints on the long-period moment-dip tradeoff for the Tohoku earthquake. *Geophys. Res. Lett.*, *38*(7), L00G17–n/a.

Universidad de Chile. (2013). *Red sismologica nacional. international federation of digital seismograph networks.* doi: https://doi.org/10.7914/SN/C1

van den Ende, M. P., & Ampuero, J.-P. (2020). On the statistical significance of foreshock sequences in southern california. *Geophysical Research Letters*, *47*(3), e2019GL086224.

Yokota, Y., & Koketsu, K. (2015). A very long-term transient event preceding the 2011 tohoku earthquake. *Nature communications*, *6*(1), 1–5.

Zhao, X., Duputel, Z., & Yao, Z. (2017). Regional w-phase source inversion for moderate to large earthquakes in china and neighboring areas. *Journal of Geophysical Research: Solid Earth*, *122*(12), 10,052-10,068. Retrieved from `https://agupubs.onlinelibrary.wiley.com/doi/abs/10.1002/2017JB014950` doi: 10.1002/2017JB014950

Zhu, L., & Rivera, L. A. (2002). A note on the dynamic and static displacements from a point source in multilayered media. *Geophysical Journal International*, *148*(3), 619–627.

Supporting Information for Seismic and aseismic fault slip during the initiation phase of the 2017 $M_W = 6.9$ Valparaíso earthquake

Emmanuel Caballero[1], Agnès Chounet[1], Zacharie Duputel[1], Jorge Jara[2],

Cedric Twardzik[1], Romain Jolivet[2,3]

[1]Institut de Physique du Globe de Strasbourg, UMR 7516, Université de Strasbourg/EOST, CNRS, Strasbourg, France.

[2]Laboratoire de Géologie, Département de Géosciences, École Normale Supérieure, PSL Université, CNRS UMR 8538, Paris, France

[3]Institut Universitaire de France, 1 rue Descartes, 75005 Paris, France

Contents of this file

1. Text S1 to S2
2. Figures S1 to S12
3. Tables S1 to S2

Introduction

S1. GPS proccesing

68 continuous GPS (cGPS) were processed in South America (66 stations) and Nazca (2 stations) Plates (Figures S1 and S2), from different networks that are listed below:

- 13 cGPS from the International GNSS service (`www.igs.org`): ANTC, AREQ, BRAZ, BRFT, CHPI, GLPS, ISPA, KOUR, LPGS, RIO2, SANT, UFPR, UNSA.
- 3 cGPS from the Instituto Geográfico Militar of Bolivia (`www.igmbolivia.gob.bo`): SCRZ, URUS, YCBA.
- 11 cGPS from the Brazilian Network (RBMC-IP, `www.ibge.gov.br`): CUIB, MABA, MSCG, NAUS, POAL, POVE, PRCV, ROCD, RSAL, SAVO, TOPL.
- 15 cGPS from Argentian National Network (RAMSAC, `www.ign.gob.ar` (Piñón et al., 2018)) AZUL, BCAR, CATA, DINO, EBYP, ESQU, MA01, NESA, PEJO, RWSN, SL01, TUCU, UNRO, UNSJ, VBCA
- 5 cGPS from the Chilean - French cooperation through LIA "Montessus de Ballore" (`www.lia-mb.net`): CONS, JRGN, OVLL, UAPE, UDAT.
- 2 cGPS from the Ministerio de Bienes Nacionales of Chile (`www.bienesnacionales .cl`): BN05, BN13
- 18 cGPS from the Centro Sismológico Nacional de Chile (CSN, `www.csn.uchile.cl` (Báez et al., 2018)): CHDA, CTPC, CUVI, DGF1, LVIL, MPLA, NAVI, PORT, QTAY, RCSD, ROB1, QTAY, SLMC, TLGT, TRPD, UAIB, VALN, ZAPA.

All these data were processed in double differences using GAMIT 10.7 software to obtain daily, 12 and 6 hours estimates of station positions, choosing ionosphere-free combination and fixing the ambiguities to integer values. The precise orbits from the International

GNSS Service for Geodynamics, precise EOPs from the IERS bulletin B, IGS tables to describe the phase centers of the antennas, FES2004 ocean-tidal loading corrections, as well as atmospheric loading corrections (tidal and non-tidal). We used precise orbits from the International GNSS Service for Geodynamics, precise EOPs from the IERS bulletin B, IGS tables to describe the phase centers of the antennas, FES2004 ocean-tidal loading corrections, as well as atmospheric loading corrections (tidal and non-tidal). One tropospheric vertical delay parameter and two horizontal gradients per stations are estimated every 2 hours. Daily solutions and position time series are combined using the PYACS software (Nocquet, 2017) in a regional stabilization process. The results are mapped into ITRF 2014 reference frame (Altamimi et al., 2016) and then put in the South-American frame using the Euler pole at $-83.4°$ E, $15.2°$ N, and angular velocity $0.287° \mathrm{my}^{-1}$ (Nocquet et al., 2014).

S2. Prediction error covariance matrix

We focus on prediction uncertainties due to inaccuracies in the Earth model. These uncertainties are represented by the matrix $\mathbf{C_p}$. We note the forward model $\mathbf{g}(\boldsymbol{\Psi}, \mathbf{m})$ for a source model $\mathbf{m}$, and Earth model parameters $\boldsymbol{\Psi}$ (i.e., P and S wave velocities, density). We can estimate $\mathbf{C_p}$ empirically from an ensemble of random models $\boldsymbol{\Psi}_\mathbf{i}, (i = 1, \ldots, n)$ as:

$$\mathbf{C_p} = \frac{1}{n-1} \sum_{i=1}^{n} (\mathbf{g}(\boldsymbol{\Psi}_\mathbf{i}, \mathbf{m}) - \bar{\mathbf{g}}(\boldsymbol{\Psi}, \mathbf{m}))(\mathbf{g}(\boldsymbol{\Psi}_\mathbf{i}, \mathbf{m}) - \bar{\mathbf{g}}(\boldsymbol{\Psi}, \mathbf{m}))^T, \tag{1}$$

where $\bar{\mathbf{g}}$ is the mean of the ensemble of predictions $\mathbf{g}(\boldsymbol{\Psi}_\mathbf{i}, \mathbf{m})$. In the following, we refer to $\mathbf{C_p}$ estimated in equation (1) as the empirical prediction error covariance matrix. Alternatively, we can compute $\mathbf{C_p}$ following a linearized perturbation approach. We assume that our forward model $\mathbf{g}(\boldsymbol{\Psi}, \mathbf{m})$ is well approximated by linearized perturbations of our predictions. For an a priori Earth model $\tilde{\boldsymbol{\Psi}}$ we write:

$$\mathbf{g}(\boldsymbol{\Psi}, \mathbf{m}) \approx \mathbf{g}(\tilde{\boldsymbol{\Psi}}, \mathbf{m}) + \mathbf{K}_{\boldsymbol{\Psi}}(\tilde{\boldsymbol{\Psi}}, \mathbf{m}) \cdot (\boldsymbol{\Psi} - \tilde{\boldsymbol{\Psi}}), \tag{2}$$

where $\mathbf{K}_{\boldsymbol{\Psi}}(\tilde{\boldsymbol{\Psi}}, \mathbf{m})$ is the sensitivity kernels of the predictions with respect to elastic parameters used to compute forward predictions:

$$\mathbf{K}_{\boldsymbol{\Psi}}(\tilde{\boldsymbol{\Psi}}, \mathbf{m}) = \frac{\partial g_i}{\partial \Psi_j}(\tilde{\boldsymbol{\Psi}}, \mathbf{m}). \tag{3}$$

In this first order approximation, we use the sensitivity kernel $\mathbf{K}_{\boldsymbol{\Psi}}(\tilde{\boldsymbol{\Psi}}, \mathbf{m})$ to estimate the covariance matrix $\mathbf{C_p}$ (Duputel et al., 2014):

$$\mathbf{C_p} = \mathbf{K}_{\boldsymbol{\Psi}} \cdot \mathbf{C}_{\boldsymbol{\Psi}} \cdot \mathbf{K}_{\boldsymbol{\Psi}}^{\mathbf{T}}, \tag{4}$$

where $\mathbf{C}_{\boldsymbol{\Psi}}$ is the covariance matrix describing uncertainty in the Earth model. To analyze both approaches, we consider a simple test case limited to an uncertain in S-wave velocity in a single layer (at 30 km depth) using the source parameters of the $M_W = 6.0$ foreshock on 2017-04-23 (see section 3 of the main text). For comparison, we calculate prediction error covariance matrices $\mathbf{C_p}$ using equation (1) and equation (4). We plot in Figure S7 the diagonal components of both matrices for a representative station. We observe that there is an overall good agreement between our first order $\mathbf{C_p}$ and the empirical $\mathbf{C_p}$ matrix. We notice some discrepancies in the variance amplitudes and a time-shift in the late part of the waveforms (after 75s in Figure S7). To explore the origin of these effects, we compare synthetic waveforms predicted from the stochastic models and the waveforms calculated with the first order approach. The results shown in Figure S8 indicate that the time-shift and amplitude difference in Figure S7 are related to the fact that the first order approach is unable to perfectly reproduce large perturbations in the Earth model.

To correct these differences, we can also estimate a covariance matrix using a second order approximation of the forward model as:

$$\mathbf{g}(\mathbf{\Psi}, \mathbf{m}) \approx \mathbf{g}(\tilde{\mathbf{\Psi}}, \mathbf{m}) + \mathbf{K_\Psi}(\tilde{\mathbf{\Psi}}, \mathbf{m}) \cdot (\mathbf{\Psi} - \tilde{\mathbf{\Psi}}) + \frac{1}{2!}\,(\mathbf{\Psi} - \tilde{\mathbf{\Psi}}) \cdot \mathbf{H_\Psi}(\tilde{\mathbf{\Psi}}, \mathbf{m}) \cdot (\mathbf{\Psi} - \tilde{\mathbf{\Psi}}), \quad (5)$$

where $\mathbf{H}_\Psi$ is the second order derivative with respect to the elastic parameters:

$$\mathbf{H_\Psi}(\tilde{\mathbf{\Psi}}, \mathbf{m}) = \frac{\partial^2 g_i}{\partial \Psi_k \partial \Psi_j}(\tilde{\mathbf{\Psi}}, \mathbf{m}). \quad (6)$$

The computation of H involves evaluating n^2 derivatives, where n is the number of elastic parameters (e.g., 3 parameters per layer for a 1D Earth model). However, assuming that cross-terms are negligible, we can reduce the number of 2nd order derivatives to be evaluated to n.

As shown in Figure S7 and S8, some of the imperfections obtained with the first order approach can be corrected by employing a second order approach neglecting cross-terms.

In practice, these discrepancies are more significant when we apply larger perturbations to the velocity model. Despite the fact that the inaccuracies of the first order approach have been corrected, we notice in Figure S8 that the differences between the first and second order approach are relatively small given the 1 Hz sampling frequency used in our moment tensor inversions. Our tests show that the differences are more visible when inverting waveforms with a higher sampling rate.

References

Altamimi, Z., Rebischung, P., Métivier, L., & Collilieux, X. (2016). ITRF2014: A new release of the International Terrestrial Reference Frame modeling nonlinear station motions. *Journal of Geophysical Research: Solid Earth*, *121*(8), 6109–6131. doi: 10.1002/2016JB013098

Báez, J. C., Leyton, F., Troncoso, C., del Campo, F., Bevis, M., Vigny, C., ... Blume, F. (2018, jul). The Chilean GNSS Network: Current Status and Progress toward Early Warning Applications. *Seismological Research Letters*, *89*(4), 1546–1554. Retrieved from `https://pubs.geoscienceworld.org/ssa/srl/article/89/4/1546/530337/The-Chilean-GNSS-Network-Current-Status-and` doi: 10.1785/0220180011

Duputel, Z., Agram, P. S., Simons, M., Minson, S. E., & Beck, J. L. (2014). Accounting for prediction uncertainty when inferring subsurface fault slip. *Geophysical Journal International*, *197*(1), 464–482.

Nocquet, J. M. (2017). Pyacs: a set of python tools for gps analysis and tectonic modelling. In *Colloque g2*.

Nocquet, J. M., Villegas-Lanza, J. C., Chlieh, M., Mothes, P. A., Rolandone, F., Jarrin, P., … Yepes, H. (2014). Motion of continental slivers and creeping subduction in the northern Andes. *Nature Geoscience*, *7*(4), 287–291. doi: 10.1038/ngeo2099

Piñón, D. A., Gómez, D. D., Smalley, R., Cimbaro, S. R., Lauría, E. A., & Bevis, M. G. (2018, mar). The History, State, and Future of the Argentine Continuous Satellite Monitoring Network and Its Contributions to Geodesy in Latin America. *Seismological Research Letters*, *89*(2A), 475–482. Retrieved from https://pubs.geoscienceworld.org/ssa/srl/article/89/2A/475/528199/The-History-State-and-Future-of-the-Argentine doi: 10.1785/0220170162

Ruiz, J. A., Contreras-Reyes, E., Ortega-Culaciati, F., & Manríquez, P. (2018). Rupture process of the april 24, 2017, mw 6.9 valparaíso earthquake from the joint inversion of teleseismic body waves and near-field data. *Physics of the Earth and Planetary Interiors*, *279*, 1–14.

Ruiz, S., Aden-Antoniow, F., Baez, J., Otarola, C., Potin, B., del Campo, F., … others (2017). Nucleation phase and dynamic inversion of the mw 6.9 valparaíso 2017 earthquake in central chile. *Geophysical Research Letters*, *44*(20), 10–290.

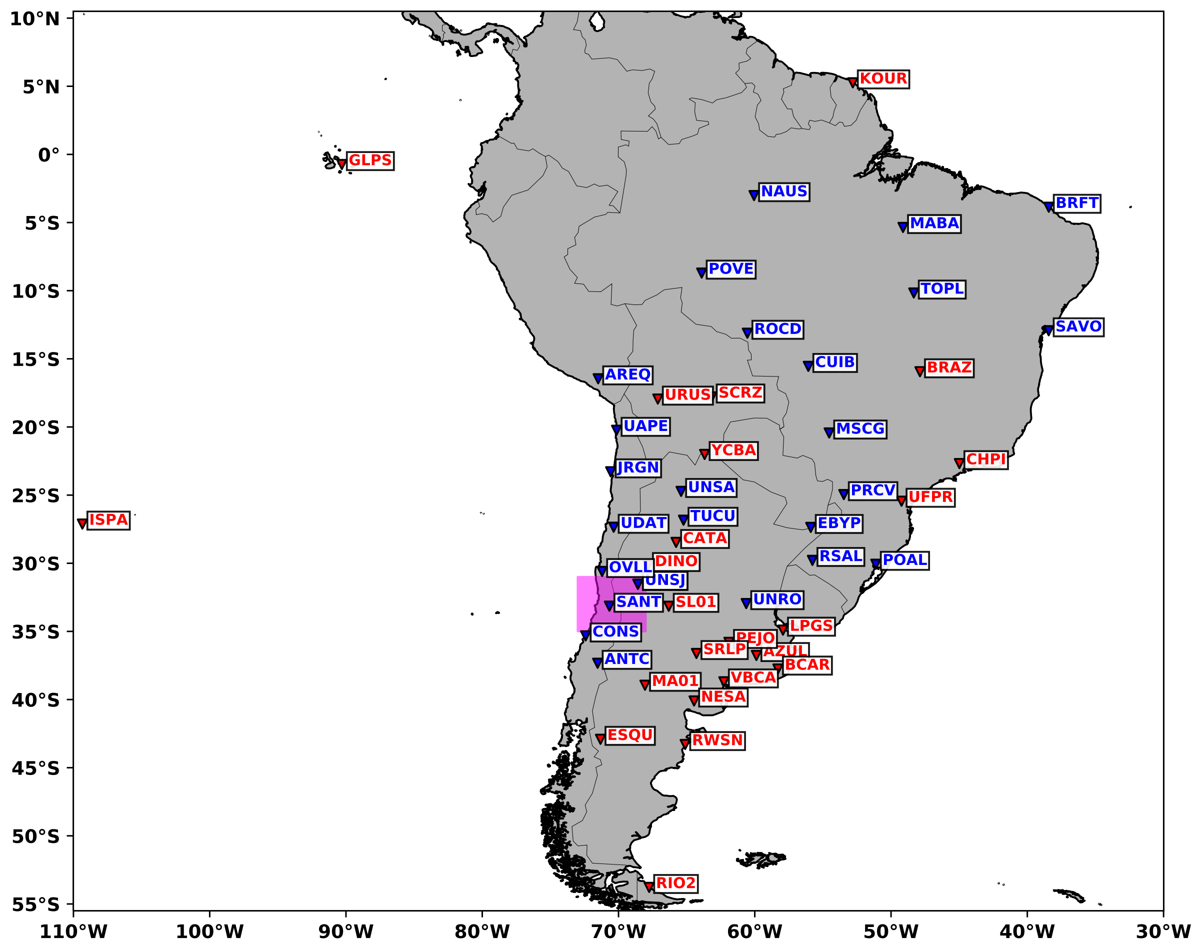

Figure S1. Map of the GPS stations processed in South America and Nazca Plates. The red stations are those ones used to define the Reference Frame, while the blue ones are just used on the processing. The pink box denotes the study area (see Figure S2 to look at the stations processed in this region).

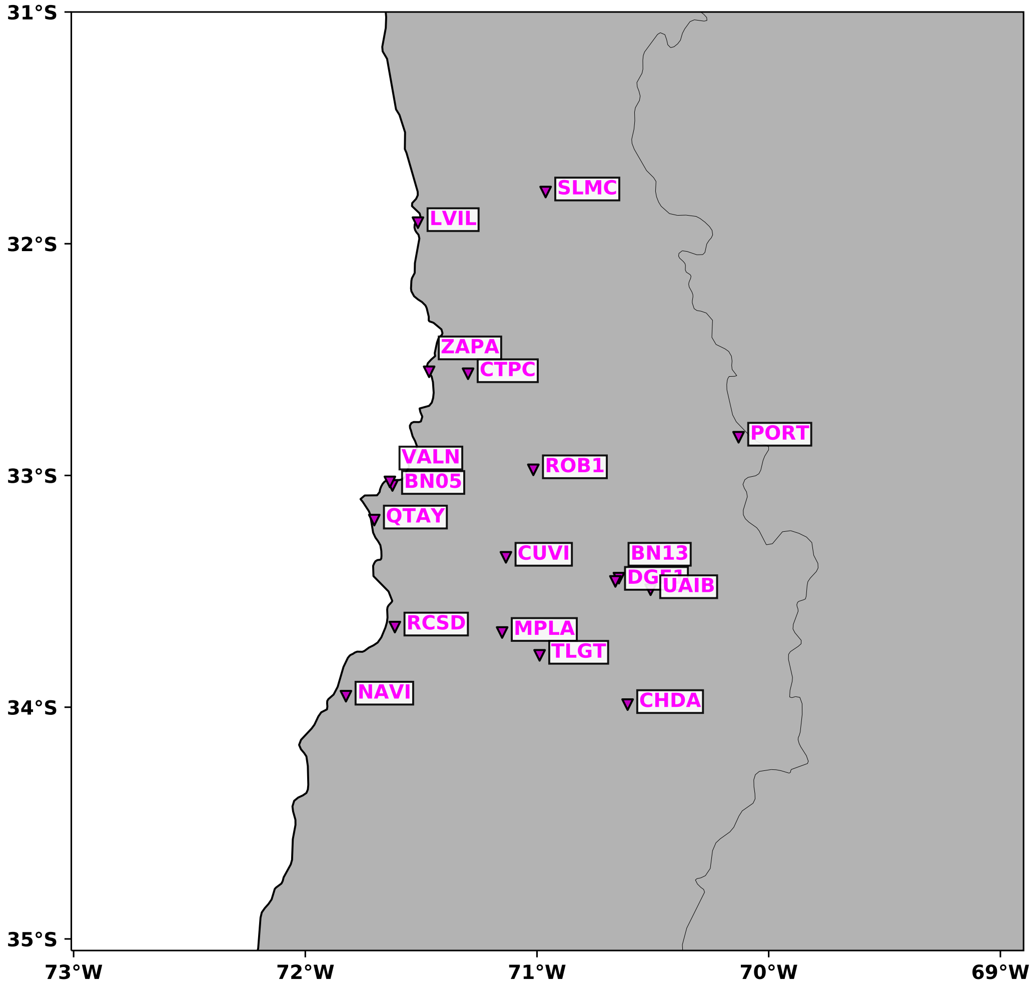

Figure S2. Map of the GPS stations processed in the study area.

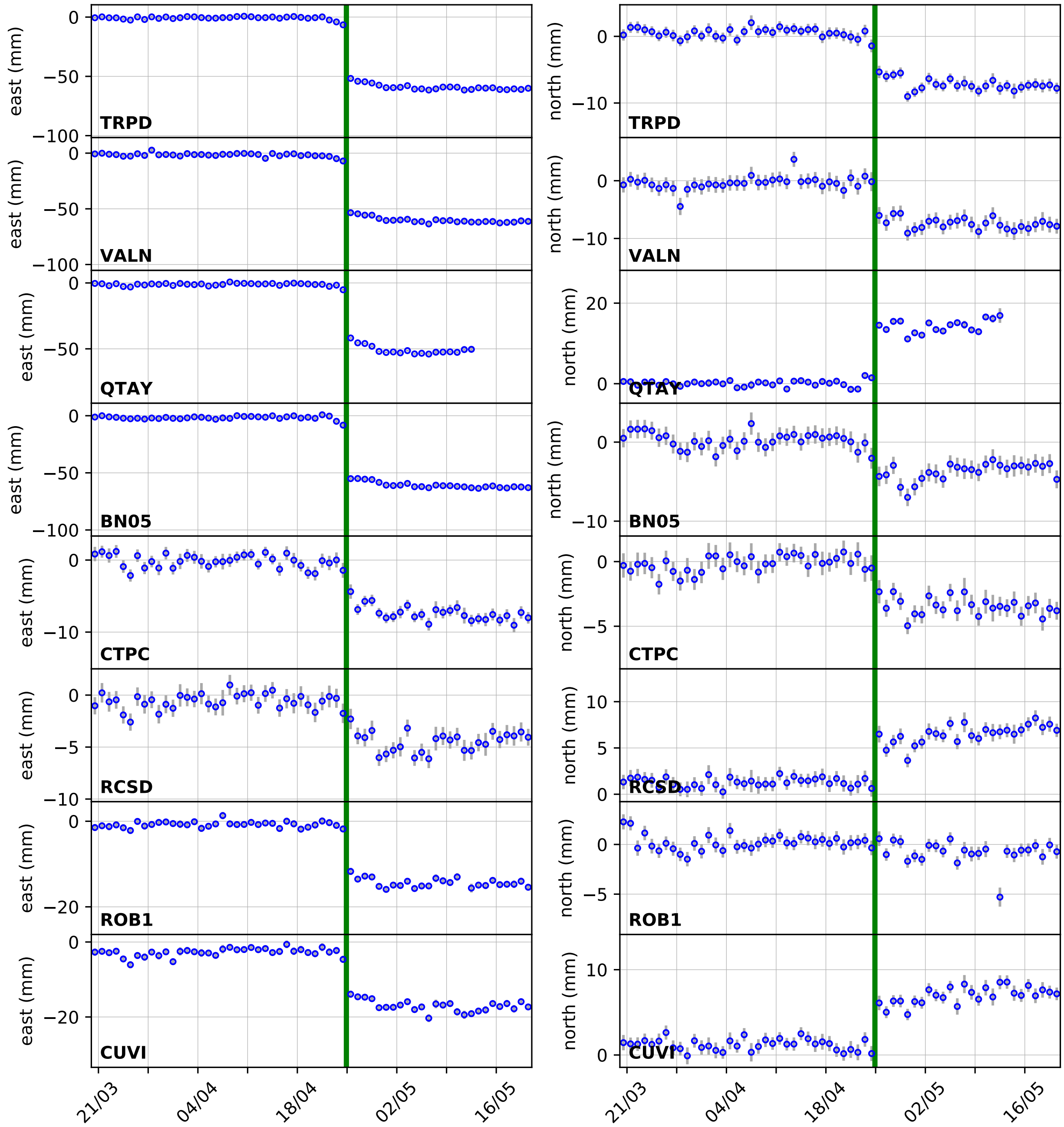

Figure S3. GPS time series for the Valparaíso region network for north and east component. The images show the time series before and after the mainshock (green line) of the sequence.

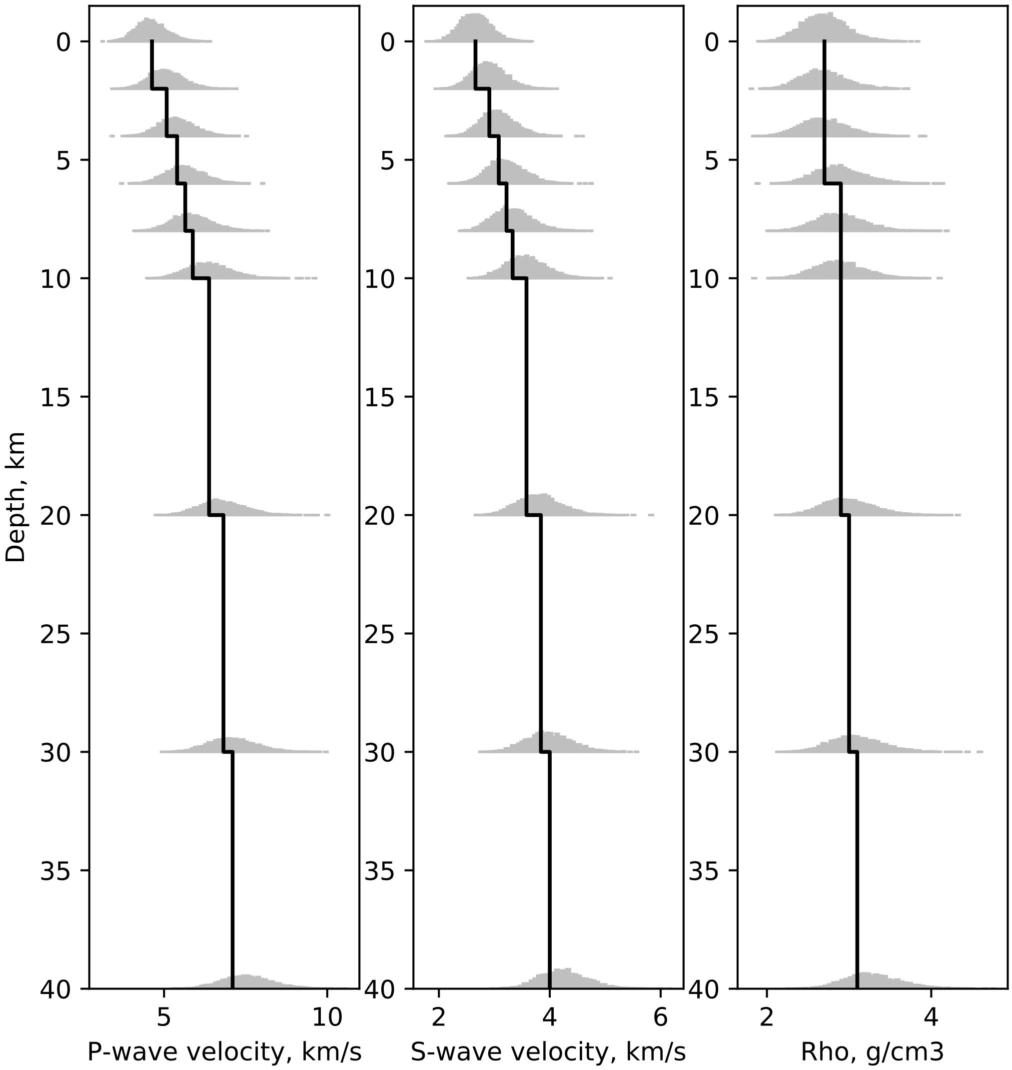

Figure S4. Model variability of the P-wave, S-wave, and density as a function of depth in Valparaíso region. Black line represents the velocity layered model used for Green's Function (GF) calculation. Grey histograms are the probability density function for each parameter as a function of depth as described in Cp.

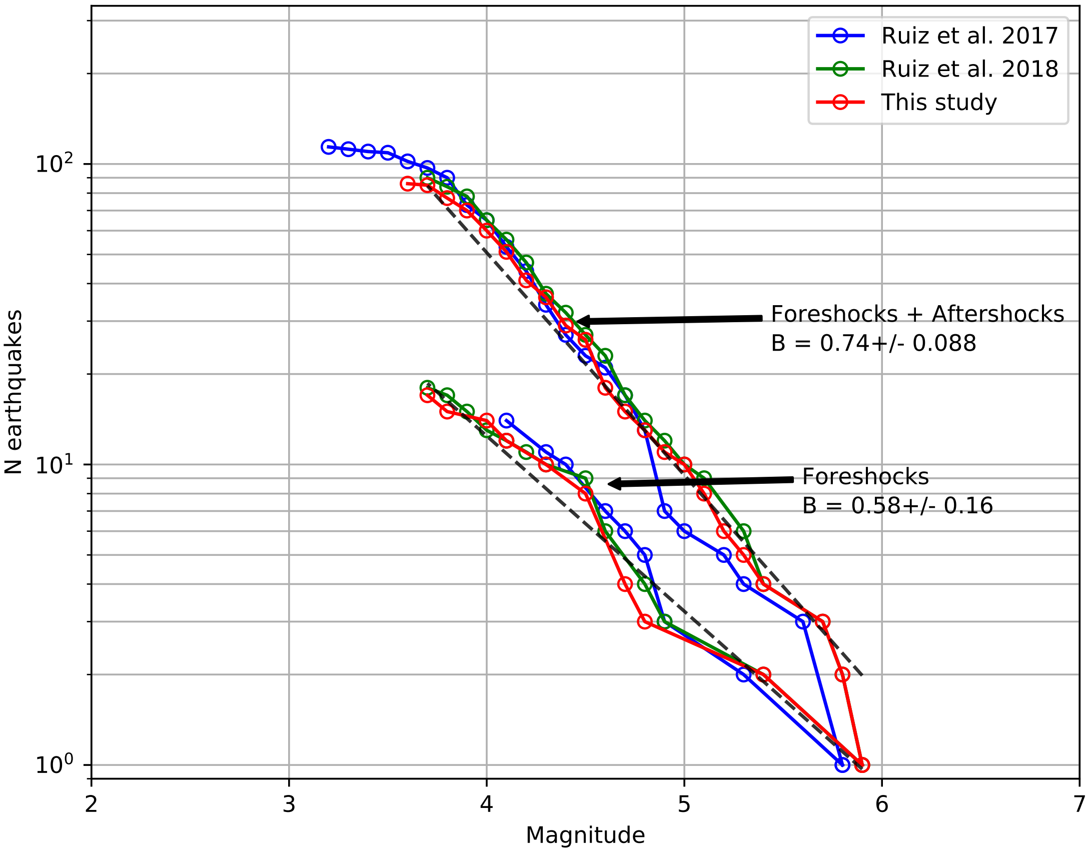

Figure S5. Gutenberg-Richter law for the 2017 Valparaíso earthquake sequence. Three different catalogs of the sequence are shown: Our CMT catalog, S. Ruiz et al. (2017) catalog, and J. A. Ruiz et al. (2018) catalog. For each catalog, both the whole sequence (foreshocks and aftershocks), and the foreshocks sequence are represented.

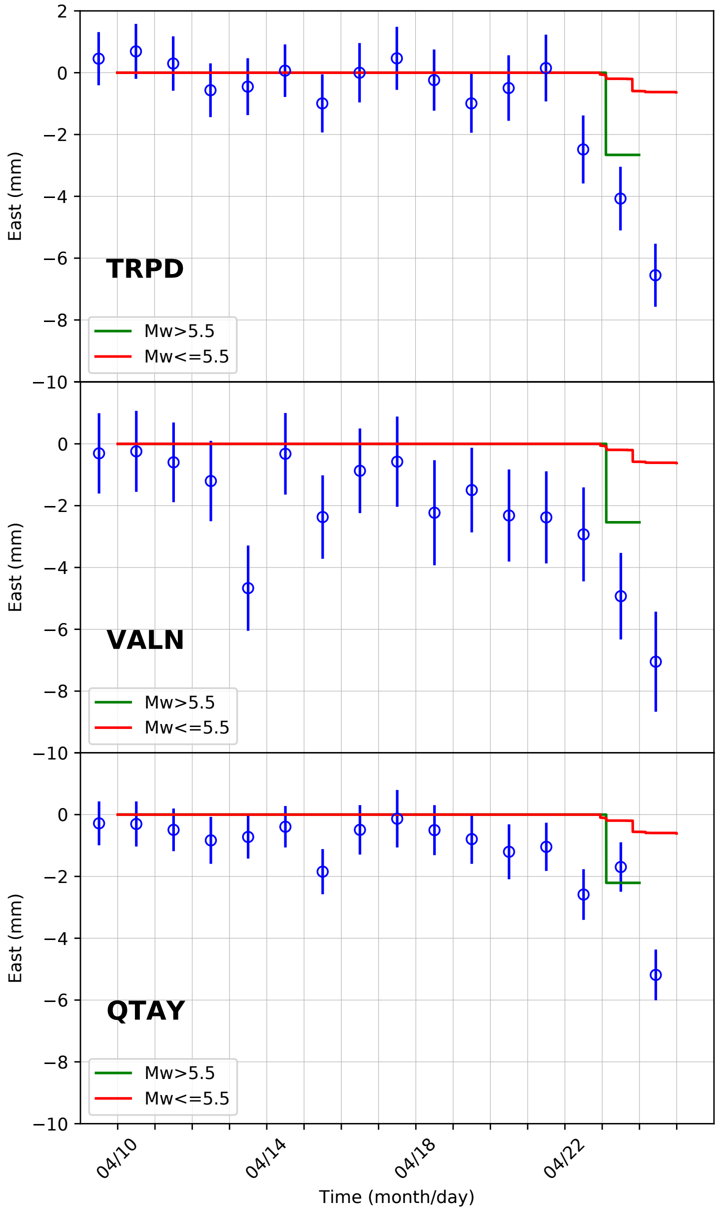

Figure S6. Synthetic surface displacement for different ranges of magnitude, foreshocks with $M_w \geq 5.5$ (largest foreshock $M_w = 6.0$) and foreshocks with $M_w \leq 5.5$. The $M_w = 6.0$ contribution appears to dominate the signal, with respect to the cumulative contribution of smaller foreshocks.

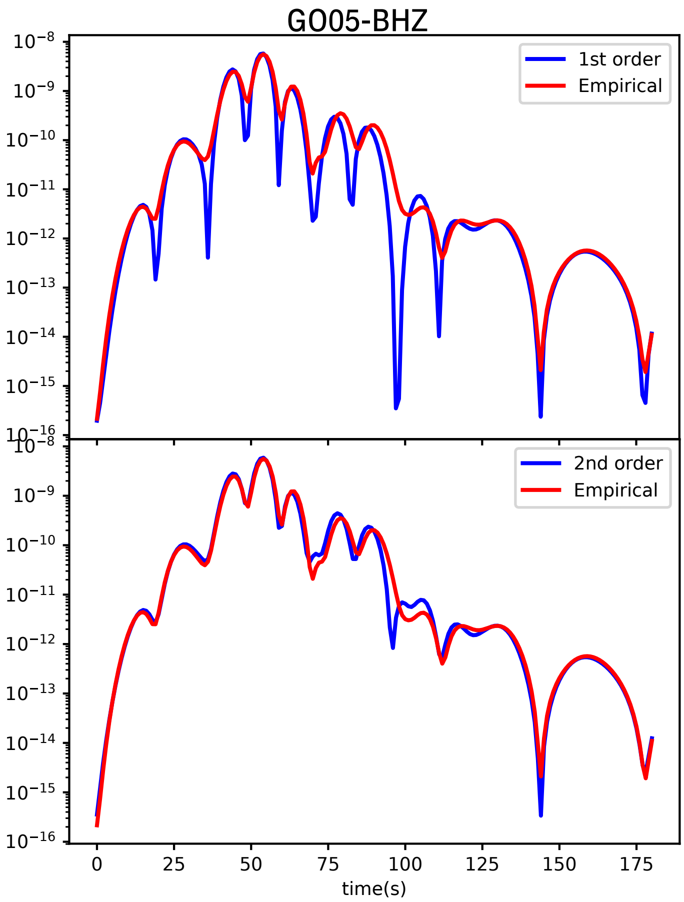

Figure S7. Diagonal of the $\mathbf{C_p}$ matrix for the vertical component of the station G005. The matrix is calculated for the $M_W = 6.0$ foreshock of the Valparaíso sequence (see section 3 of the main text). The red line represents the diagonal matrix for the empirical covariance matrix (i.e., the matrix created from an ensemble of models). The blue line represents the first (top) and second-order (bottom) approaches used to compute $\mathbf{C_p}$.

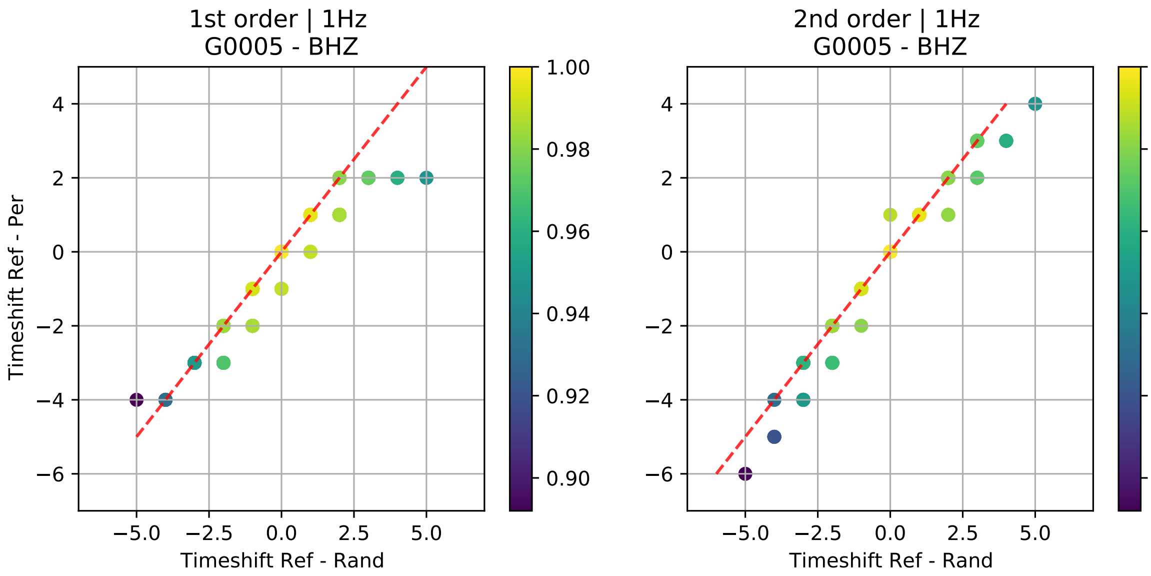

Figure S8. Comparison between synthetic waveforms predicted from stochastic models calculated with a log-normal distribution, and synthetic waveforms calculated using the first and second order $\mathbf{C_p}$ matrix. The waveforms are generated using the source model of the $M_W = 6.0$ foreshock presented in section 3 of the main text. The X-axis represents time shifts between waveforms generated with the average velocity model of the region (figure S4) and waveform predicted for randomly perturbed velocity models. The Y-axis represents time shifts between waveforms generated with the average velocity model and waveforms generated either with the first or the second order approximation (see equations (2) and (5) of text S2). The color represents the correlation coefficient of each pair of waveforms. If the comparison follows the $y = x$ line, it means that the perturbation approximation properly estimates the empirical covariance matrix. We can observe that the second order approach better approximates actual synthetics (especially when there is a significant time-delay between waveforms).

OFF_COAST_CENTRAL_CHILE, filter = (0.01, 0.04, 4, 1), p 1/4

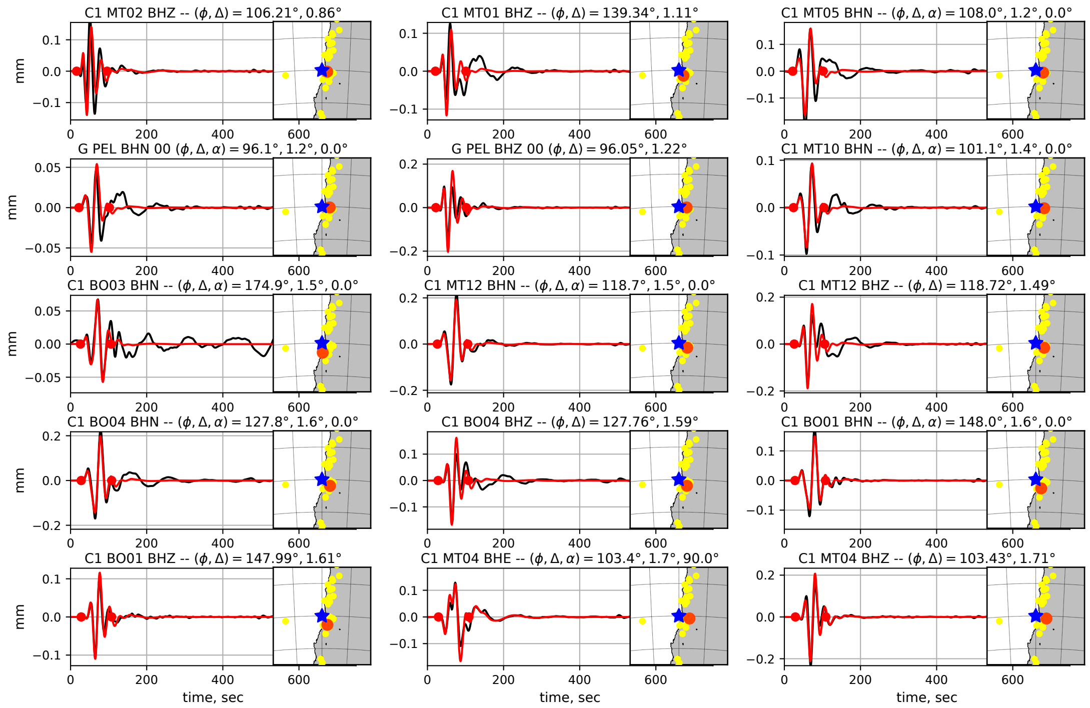

OFF_COAST_CENTRAL_CHILE, filter = (0.01, 0.04, 4, 1), p 2/4

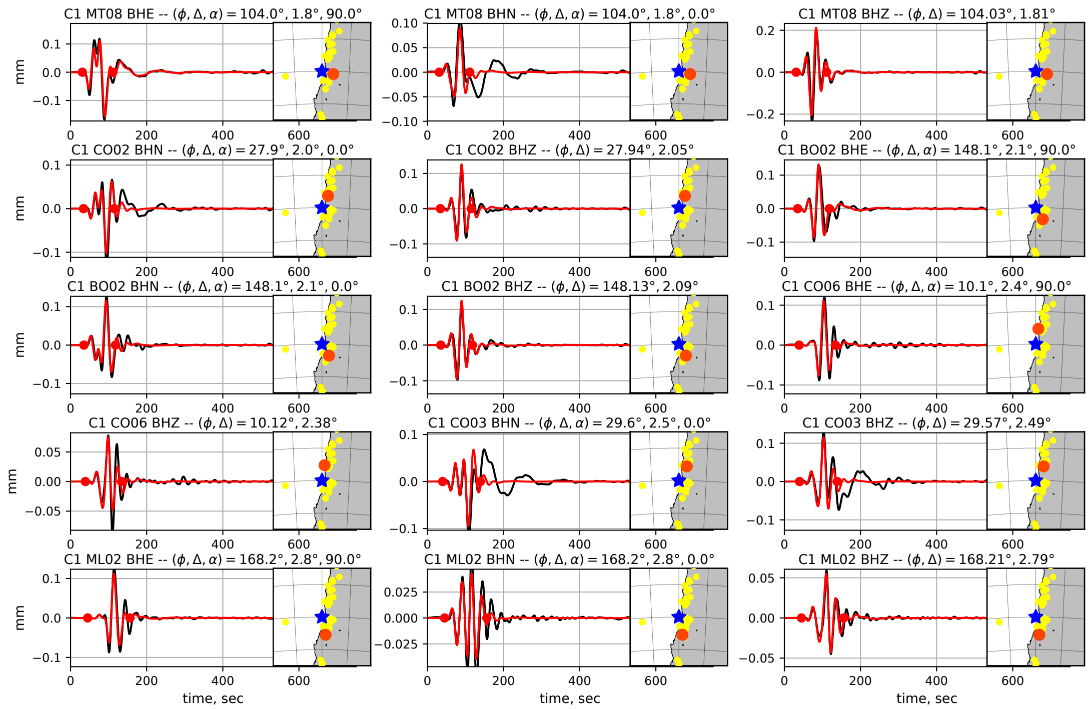

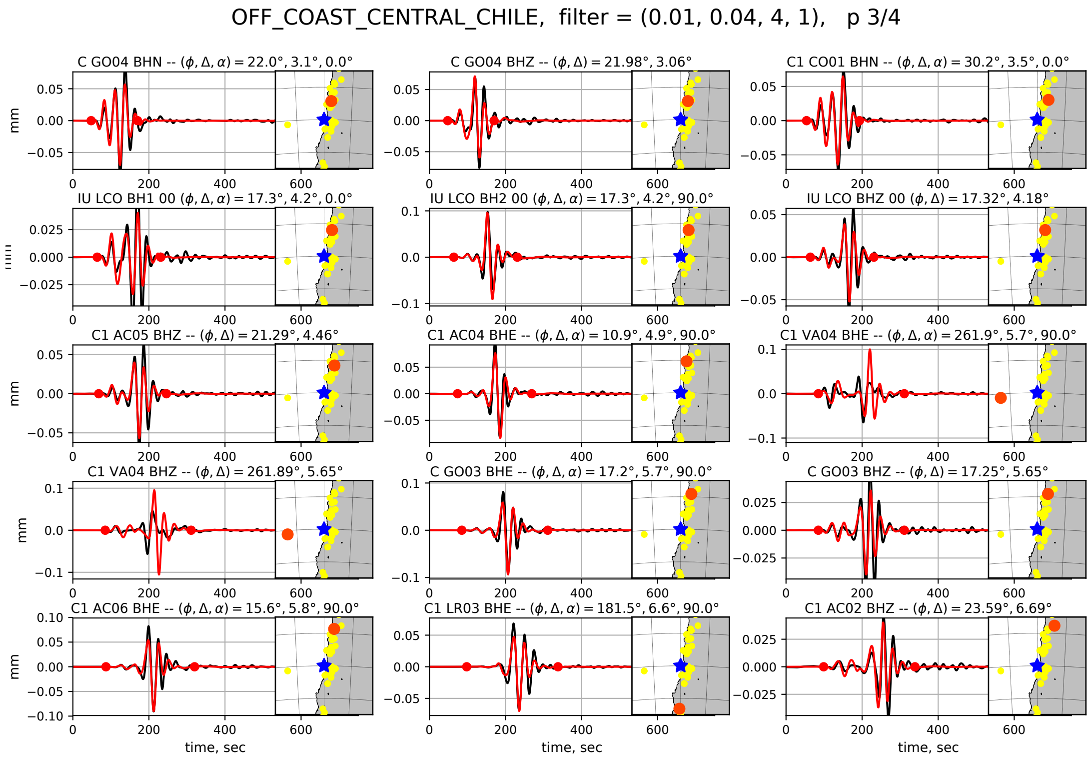

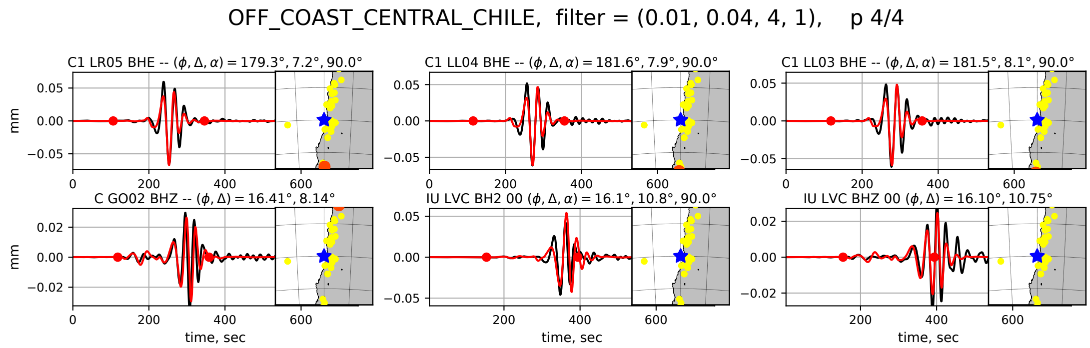

Figure S9. Waveforms fit for the $M_W = 6.0$ foreshock using CMT solution from our catalog. Observed (black) and synthetic (red) waveforms for a given station (orange). The fit (inversion) is made between red dots. The blue star represents the CMT location. Yellow dots correspond to the ensemble of stations used in the inversion.

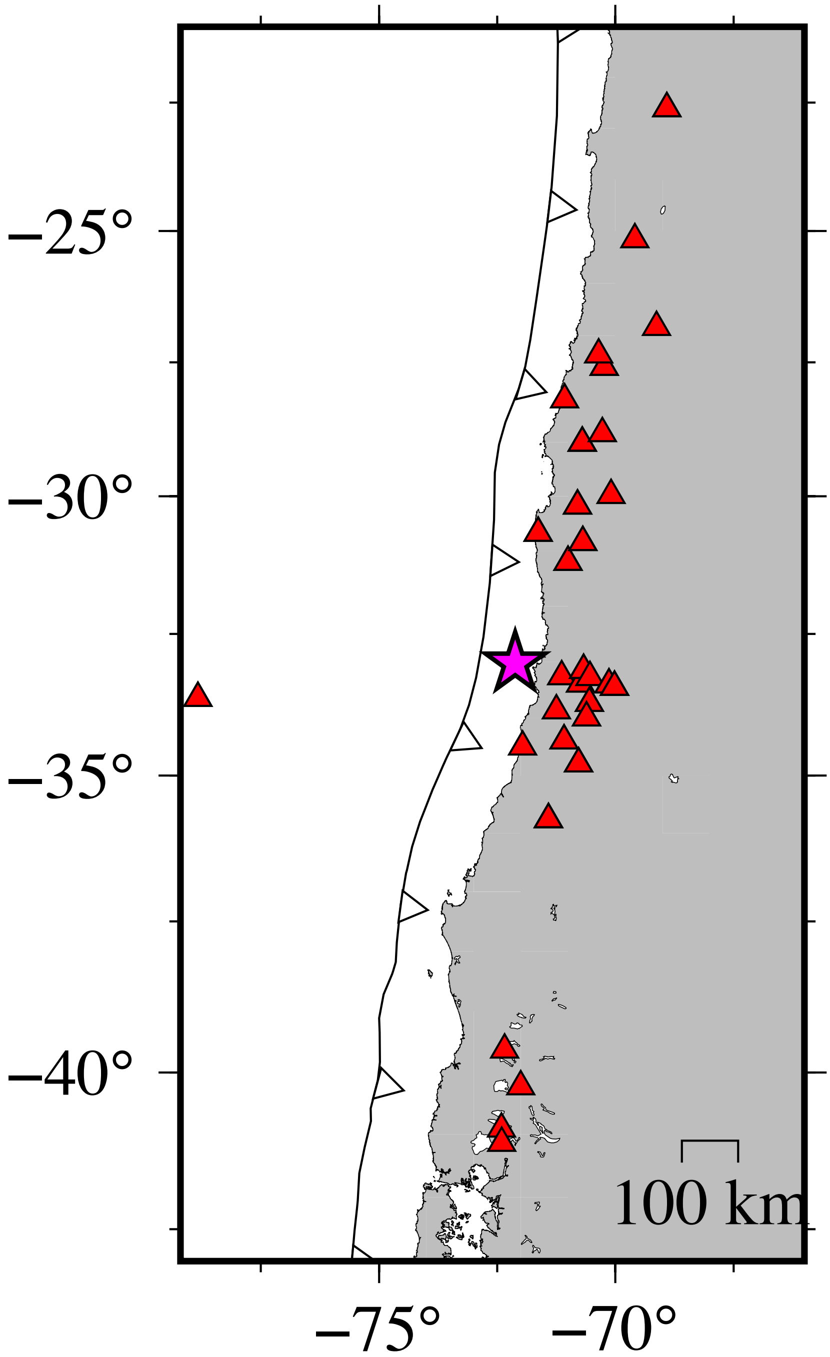

Figure S10. Stations used for the $M_W = 6$ foreshock CMT inversion. The CMT location is shown in purple.

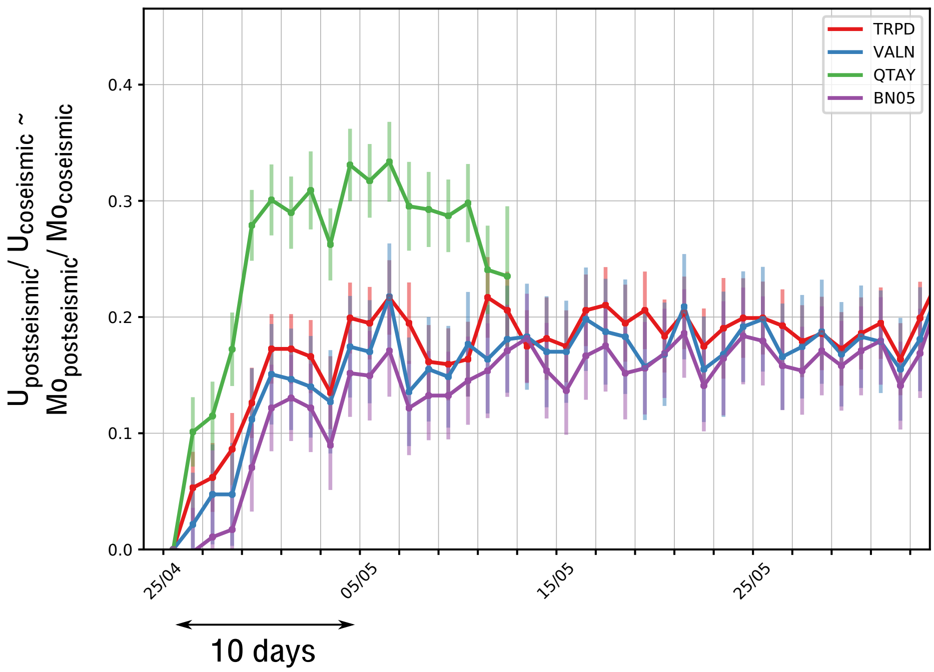

Figure S11. Mainshock postseismic surface displacement normalized by the coseismic displacement at each GPS station. This ratio approximates the moment ratio between postseismic and coseismic terms.

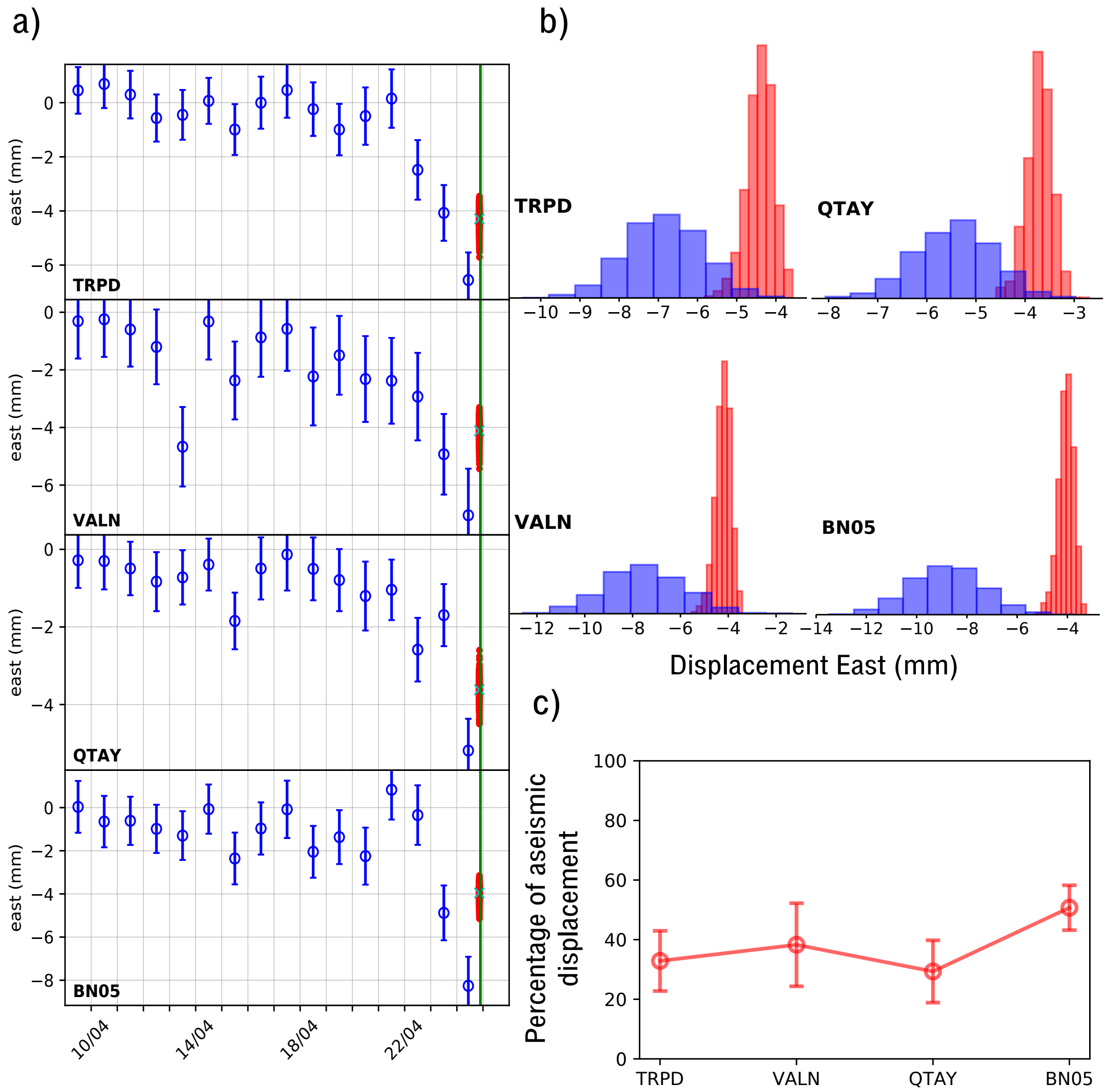

Figure S12. Same as Figure 4 of main text but with the quick postseismic contribution produced by the largest foreshock.

Table S1. Bandpass filter corner frequencies used for CMT inversion

Magnitude	Low Corner Freq (Hz)	High Corner Freq (Hz)
< 4.5	0.02	0.08
> 4.5	0.015	0.06
6.0	0.01	0.04

Table S2: CMT solutions of our catalog.

Date	Time	Lon °	Lat °	Depth km	M0 N·m	Mw	Mrr N·m	Mtt N·m	Mpp N·m	Mrt N·m	Mrp N·m	Mtp N·m
2017-04-15	01:50:23	-70.85	-31.93	35.5	3.56e+14	3.63	-1.49e+20	-8.60e+20	1.01e+21	-1.82e+20	-1.83e+21	2.927e+21
2017-04-22	22:46:44	-71.96	-33.14	17.5	2.21e+16	4.83	1.76e+23	-1.58e+22	-1.60e+23	-2.78e+22	-1.41e+23	3.324e+21
2017-04-22	23:57:13	-72.03	-33.05	21.5	2.10e+15	4.15	1.28e+22	-1.07e+21	-1.17e+22	-8.45e+20	-1.70e+22	9.225e+20
2017-04-23	01:49:12	-72.06	-33.03	22.5	8.47e+15	4.55	5.58e+22	2.57e+21	-5.83e+22	-5.42e+21	-6.24e+22	9.259e+20
2017-04-23	02:36:06	-72.10	-33.03	19.5	1.16e+18	6.0	7.45e+24	-3.96e+23	-7.05e+24	4.10e+23	-9.06e+24	-5.981e+22
2017-04-23	02:43:18	-71.89	-33.05	21.5	1.76e+16	4.76	7.84e+22	2.41e+22	-1.03e+23	-1.86e+22	-1.44e+23	-4.994e+22
2017-04-23	02:52:38	-72.00	-33.05	25.5	8.02e+15	4.54	6.41e+22	-5.19e+20	-6.36e+22	1.29e+21	-4.66e+22	-1.311e+22
2017-04-23	03:00:12	-71.97	-32.86	14.5	5.04e+15	4.40	3.97e+22	-7.83e+21	-3.19e+22	-9.10e+21	-3.43e+22	4.470e+21
2017-04-23	03:02:17	-72.02	-33.07	26.5	8.48e+15	4.55	7.48e+22	-5.13e+21	-6.97e+22	6.45e+21	-4.39e+22	-2.778e+21
2017-04-23	12:52:15	-71.99	-33.07	26.5	5.42e+14	3.76	3.07e+21	2.78e+20	-3.34e+21	4.33e+20	-4.30e+21	-6.063e+20
2017-04-23	16:12:54	-71.96	-32.99	25.5	1.93e+15	4.12	1.12e+22	-2.14e+21	-9.07e+21	-7.36e+20	-1.63e+22	-9.098e+20
2017-04-23	19:40:10	-72.16	-33.05	21.5	2.10e+17	5.5	1.69e+24	-1.06e+23	-1.59e+24	5.75e+22	-1.31e+24	8.445e+22
2017-04-23	20:30:50	-72.10	-33.06	30.5	1.50e+15	4.05	5.58e+21	1.06e+22	-1.62e+22	2.95e+21	-5.86e+21	-3.027e+20
2017-04-24	01:19:42	-72.04	-33.11	22.5	1.31e+15	4.01	6.16e+21	9.72e+20	-7.14e+21	4.68e+20	-1.12e+22	-1.181e+21
2017-04-24	03:50:50	-72.14	-33.09	24.5	4.53e+15	4.37	3.42e+22	-3.71e+21	-3.05e+22	3.65e+21	-3.11e+22	4:655e+21
2017-04-24	03:54:11	-72.05	-33.10	21.5	7.87e+15	4.53	5.58e+22	-2.75e+21	-5.30e+22	8.92e+21	-5.55e+22	-8.387e+21
2017-04-24	06:54:36	-72.06	-33.11	23.5	7.69e+14	3.86	4.85e+21	-7.75e+20	-4.07e+21	1.17e+21	-6.13e+21	4.638e+20
2017-04-24	13:17:02	-71.93	-33.00	28.5	5.03e+14	3.73	2.19e+21	1.04e+21	-3.23e+21	-7.60e+18	-4.09e+21	-1.127e+21
2017-04-24	23:54:45	-71.93	-33.29	35.5	1.43e+16	4.70	5.65e+22	3.38e+22	-9.04e+22	2.77e+22	-1.16e+23	-1.953e+22
2017-04-25	00:17:36	-72.04	-33.17	20.5	7.58e+15	4.52	6.05e+22	-5.41e+21	-5.51e+22	-5.64e+21	-4.85e+22	5.282e+21
2017-04-25	01:33:15	-72.04	-33.16	22.5	1.56e+16	4.73	1.27e+23	-3.88e+21	-1.23e+23	1.73e+22	-9.06e+22	6.894e+21
2017-04-25	01:43:03	-72.09	-33.16	22.5	6.78e+16	5.15	5.20e+23	-3.77e+22	-4.82e+23	2.10e+22	-4.56e+23	5.773e+21
2017-04-25	01:54:30	-72.11	-33.10	22.5	1.45e+15	4.04	2.60e+21	2.37e+21	-4.97e+21	8.85e+20	-1.22e+22	-6.659e+21
2017-04-25	02:33:05	-71.89	-33.00	32.5	9.88e+14	3.93	8.24e+21	-2.88e+21	-5.36e+21	1.11e+21	-7.10e+21	-3.851e+20
2017-04-25	03:02:23	-72.08	-33.16	23.5	9.33e+15	4.58	7.71e+22	-1.13e+22	-6.58e+22	8.15e+21	-5.93e+22	3.680e+21
2017-04-25	05:56:26	-72.28	-33.03	17.5	2.43e+15	4.19	2.26e+22	-5.64e+21	-1.70e+22	-6.61e+19	-1.27e+22	4.963e+21
2017-04-25	06:34:15	-71.93	-32.97	25.5	4.88e+14	3.73	3.60e+21	-5.02e+20	-3.10e+21	-6.10e+20	-3.50e+21	4.637e+19
2017-04-25	08:15:17	-71.98	-32.97	24.5	9.43e+14	3.92	5.98e+21	-5.54e+20	-5.43e+21	1.41e+20	-7.48e+21	-6.557e+20
2017-04-25	08:29:06	-72.09	-33.15	19.5	1.21e+15	3.99	8.03e+21	7.54e+20	-8.78e+21	3.61e+20	-8.67e+21	-1.002e+20
2017-04-25	09:33:31	-72.00	-33.10	27.5	3.85e+15	4.32	2.18e+22	-3.06e+21	-1.87e+22	5.88e+21	-3.20e+22	-3.549e+21
2017-04-25	10:20:23	-72.11	-32.92	21.5	1.95e+15	4.13	8.25e+21	-2.08e+20	-8.04e+21	-1.85e+21	-1.76e+22	-2.089e+20

Continued on next page

Table S2 – *Continued from previous page*

Date	Time	Lon °	Lat °	Depth km	M0 N·m	Mw	Mrr N·m	Mtt N·m	Mpp N·m	Mrt N·m	Mrp N·m	Mtp N·m
2017-04-25	10:24:35	-72.14	-32.90	22.5	2.28e+15	4.17	1.90e+22	-2.81e+21	-1.62e+22	-1.29e+21	-1.43e+22	-2.237e+21
2017-04-25	11:22:02	-72.20	-33.03	19.5	1.03e+15	3.94	8.45e+21	-1.21e+21	-7.24e+21	3.36e+19	-6.50e+21	1.057e+21
2017-04-25	11:24:09	-72.27	-33.12	19.5	1.70e+15	4.09	1.50e+22	-2.19e+21	-1.28e+22	3.35e+21	-9.24e+21	2.462e+20
2017-04-25	12:13:23	-72.21	-33.12	19.5	1.21e+16	4.65	1.02e+23	-1.01e+22	-9.21e+22	1.81e+22	-6.92e+22	2.311e+21
2017-04-25	12:37:37	-72.16	-33.05	21.5	1.31e+15	4.01	8.31e+21	-3.74e+20	-7.94e+21	1.08e+20	-1.02e+22	1.217e+21
2017-04-25	14:26:35	-72.10	-33.17	21.5	2.76e+15	4.23	1.34e+22	7.15e+20	-1.41e+22	2.13e+21	-2.37e+22	2.934e+21
2017-04-25	15:32:07	-72.21	-33.10	19.5	1.18e+15	3.98	1.15e+22	-2.05e+21	-9.41e+21	-5.21e+20	-4.93e+21	2.174e+21
2017-04-25	16:38:53	-72.18	-33.07	19.5	1.41e+15	4.03	9.02e+21	4.71e+20	-9.49e+21	4.63e+20	-1.06e+22	-5.471e+20
2017-04-25	16:48:36	-72.01	-33.31	24.5	1.99e+15	4.13	9.15e+21	6.87e+20	-9.84e+21	7.19e+21	-1.58e+22	1.966e+21
2017-04-25	20:57:54	-72.15	-33.13	19.5	1.16e+15	3.98	9.76e+21	-9.29e+20	-8.83e+21	1.11e+21	-6.90e+21	-3.074e+19
2017-04-25	21:03:13	-72.06	-33.12	17.5	8.67e+14	3.89	6.93e+21	-2.24e+21	-4.69e+21	1.96e+21	-6.05e+21	6.534e+20
2017-04-25	23:58:11	-71.98	-32.95	26.5	1.25e+15	4.00	1.04e+22	-1.85e+21	-8.51e+21	1.59e+20	-8.10e+21	1.225e+21
2017-04-26	00:43:00	-71.96	-32.94	26.5	4.63e+14	3.71	1.77e+21	2.60e+20	-2.03e+21	-4.96e+20	-4.19e+21	-5.287e+19
2017-04-26	10:05:34	-72.21	-33.14	21.5	4.05e+15	4.34	3.21e+22	-3.83e+21	-2.82e+22	6.22e+21	-2.64e+22	1.765e+20
2017-04-26	14:45:55	-71.85	-33.29	27.5	4.49e+15	4.37	3.33e+22	-2.38e+20	-3.31e+22	3.36e+21	-3.00e+22	1.143e+21
2017-04-26	15:14:01	-71.99	-33.30	31.5	4.64e+15	4.38	3.80e+22	7.82e+20	-3.88e+22	9.17e+21	-2.42e+22	2.401e+21
2017-04-27	01:55:05	-71.81	-33.13	32.5	1.05e+15	3.95	9.92e+21	-3.26e+20	-9.59e+21	9.98e+20	-3.61e+21	1.043e+21
2017-04-27	05:09:22	-71.90	-33.31	27.5	4.06e+16	5.01	3.31e+23	1.23e+22	-3.43e+23	8.57e+21	-2.13e+23	7.488e+22
2017-04-27	06:55:45	-71.88	-33.29	25.5	1.86e+15	4.11	1.23e+22	-7.08e+20	-1.16e+22	1.08e+21	-1.42e+22	-1.304e+20
2017-04-27	08:24:41	-71.89	-33.28	28.5	1.34e+16	4.68	1.04e+23	7.86e+21	-1.12e+23	6.07e+21	-7.88e+22	3.411e+21
2017-04-27	08:46:34	-72.06	-33.10	23.5	1.70e+15	4.09	8.60e+21	-5.83e+20	-8.01e+21	1.44e+21	-1.47e+22	-4.253e+20
2017-04-27	21:17:33	-71.92	-33.30	29.5	8.93e+14	3.90	5.29e+21	1.21e+21	-6.50e+21	2.02e+20	-6.69e+21	-4.765e+20
2017-04-28	15:30:05	-72.02	-33.26	23.5	7.43e+17	5.85	5.32e+24	-2.17e+23	-5.10e+24	1.60e+24	-5.03e+24	5.323e+23
2017-04-28	15:33:30	-71.96	-33.32	23.5	2.32e+16	4.84	1.72e+23	-1.56e+22	-1.57e+23	4.19e+22	-1.58e+23	-1.243e+22
2017-04-28	15:40:24	-71.91	-33.26	28.5	8.66e+15	4.56	4.40e+22	1.25e+22	-5.65e+22	4.84e+22	-4.91e+22	-2.064e+22
2017-04-28	15:49:44	-71.91	-33.31	26.5	2.89e+16	4.91	1.74e+23	2.36e+22	-1.98e+23	3.56e+22	-2.18e+23	1.129e+22
2017-04-28	15:58:34	-72.05	-33.26	27.5	1.32e+17	5.35	9.24e+23	-2.51e+22	-8.98e+23	3.88e+23	-8.39e+23	2.300e+23
2017-04-28	16:05:57	-71.66	-33.17	29.5	5.06e+17	5.74	3.37e+24	-4.38e+23	-2.93e+24	-6.71e+23	-3.88e+24	5.465e+23
2017-04-28	17:09:40	-71.93	-33.25	20.5	7.87e+15	4.53	2.26e+22	1.64e+22	-3.91e+22	2.52e+22	-6.67e+22	-3.073e+21
2017-04-28	17:21:48	-72.06	-33.23	24.5	3.25e+15	4.27	1.51e+22	2.05e+21	-1.72e+22	9.80e+21	-2.64e+22	-6.374e+19
2017-04-28	17:38:09	-71.93	-33.35	29.5	4.21e+15	4.35	-1.54e+22	-8.40e+21	2.38e+22	2.62e+22	-8.34e+21	-2.420e+22
2017-04-28	17:41:50	-71.98	-33.30	25.5	1.11e+17	5.30	7.98e+23	-2.82e+22	-7.70e+23	2.17e+21	-7.79e+23	-3.052e+22

Continued on next page

Table S2 – *Continued from previous page*

Date	Time	Lon °	Lat °	Depth km	M0 N·m	Mw	Mrr N·m	Mtt N·m	Mpp N·m	Mrt N·m	Mrp N·m	Mtp N·m
2017-04-28	17:57:07	-71.94	-33.36	30.5	2.57e+15	4.21	1.60e+22	1.97e+21	-1.79e+22	-3.88e+21	-1.88e+22	3.429e+20
2017-04-28	18:28:23	-71.96	-33.28	29.5	2.68e+15	4.22	1.30e+22	9.66e+20	-1.39e+22	3.90e+21	-2.28e+22	-1.247e+21
2017-04-29	01:06:23	-72.02	-33.25	20.5	4.87e+14	3.73	1.49e+21	1.13e+21	-2.63e+21	2.44e+21	-3.40e+21	-1.148e+21
2017-04-29	01:08:35	-71.99	-33.37	27.5	5.34e+15	4.42	3.22e+22	2.74e+21	-3.49e+22	-3.80e+21	-4.03e+22	-9.976e+21
2017-04-29	01:37:16	-72.07	-33.23	25.5	5.16e+15	4.41	3.27e+22	4.71e+21	-3.74e+22	2.14e+22	-3.01e+22	7.211e+21
2017-04-29	01:46:00	-72.02	-33.22	24.5	5.41e+16	5.09	4.98e+23	-4.40e+22	-4.54e+23	8.74e+22	-2.43e+23	1.079e+22
2017-04-29	02:36:24	-71.73	-33.12	32.5	7.30e+14	3.84	7.48e+21	-1.76e+21	-5.71e+21	-7.30e+20	2.43e+21	1.489e+21
2017-04-29	04:50:34	-72.07	-33.24	22.5	7.66e+14	3.86	4.21e+21	-9.67e+19	-4.11e+21	3.07e+21	-5.62e+21	6.726e+20
2017-04-29	08:30:43	-72.05	-33.25	24.5	2.92e+15	4.24	8.79e+21	7.25e+21	-1.60e+22	1.38e+22	-2.17e+22	-1.908e+20
2017-04-29	08:54:02	-72.03	-33.24	22.5	2.54e+15	4.20	6.44e+21	4.24e+21	-1.07e+22	8.88e+21	-2.20e+22	1.113e+20
2017-04-30	17:55:34	-72.02	-33.37	26.5	8.74e+14	3.89	5.89e+21	-2.22e+20	-5.67e+21	-6.18e+20	-5.07e+21	-4.335e+21
2017-04-30	21:49:02	-72.26	-32.97	22.5	1.04e+15	3.95	1.05e+22	-1.74e+21	-8.73e+21	4.23e+20	-4.01e+21	-3.070e+20
2017-05-01	23:38:45	-72.21	-33.01	18.5	1.79e+15	4.10	1.49e+22	-1.38e+21	-1.35e+22	1.76e+21	-1.07e+22	-1.596e+20
2017-05-03	16:50:22	-72.26	-33.08	21.5	5.62e+15	4.43	5.74e+22	-1.11e+22	-4.63e+22	2.43e+21	-2.16e+22	1.035e+21
2017-05-04	14:31:43	-72.15	-33.09	22.5	5.62e+14	3.77	4.83e+21	-2.63e+20	-4.57e+21	6.57e+20	-2.99e+21	3.640e+20
2017-05-05	01:34:46	-72.24	-32.90	18.5	1.04e+15	3.95	6.92e+21	5.61e+20	-7.48e+21	8.32e+20	-7.45e+21	9:744e+20
2017-05-05	04:42:01	-71.99	-32.82	22.5	4.92e+14	3.73	2.14e+21	8.61e+19	-2.23e+21	9.84e+20	-4.22e+21	8.527e+20
2017-05-05	10:48:21	-72.18	-32.94	16.5	6.36e+14	3.80	5.53e+21	-1.53e+20	-5.37e+21	1.07e+21	-3.11e+21	-1.131e+20
2017-05-09	09:22:31	-72.27	-33.75	21.5	7.49e+14	3.85	5.79e+21	1.88e+20	-5.98e+21	-4.60e+19	-4.54e+21	9.364e+20
2017-05-09	11:28:32	-72.25	-33.05	19.5	4.44e+14	3.70	4.06e+21	-9.09e+20	-3.15e+21	1.48e+19	-2.55e+21	4.498e+20
2017-05-13	16:54:46	-72.06	-32.94	26.5	6.48e+16	5.14	5.42e+23	-3.86e+22	-5.04e+23	-5.74e+22	-3.78e+23	-6.968e+21
2017-05-16	02:16:29	-72.21	-32.96	16.5	1.99e+15	4.13	-2.93e+21	1.90e+21	1.03e+21	3.93e+21	-1.01e+22	-1.707e+22
2017-05-16	04:36:15	-71.65	-32.00	27.5	4.20e+15	4.35	1.60e+21	9.87e+20	-2.59e+21	2.57e+20	-4.18e+22	3.070e+21
2017-05-18	00:44:56	-72.32	-33.03	17.5	2.20e+15	4.16	2.37e+22	-3.86e+21	-1.98e+22	7.27e+20	-2.60e+21	1.786e+21
2017-05-23	01:05:12	-72.16	-32.94	19.5	1.61e+15	4.07	6.78e+21	-7.61e+20	-6.02e+21	9.26e+21	1.18e+22	1.183e+21
2017-05-29	20:39:36	-71.86	-32.16	26.5	5.78e+14	3.77	-2.65e+21	2.71e+21	-6.71e+19	-1.05e+21	-5.11e+21	1.094e+21
2017-05-30	06:45:58	-72.19	-32.98	18.5	8.59e+14	3.89	7.53e+21	-1.20e+21	-6.34e+21	1.74e+21	-4.68e+21	7.912e+20